Technical Report for the Analysis of $\bar{p}p \rightarrow \pi^0\pi^0\pi^0\eta$ at 1.94GeV/c

Andy Cooper

DRAL

UK

August 22, 1994

Abstract

Crystal Barrel $\bar{p}p \to \pi\pi\pi\eta$ data at 1.20GeV/c and 1.94GeV/c have been analysed. In the $\pi^0\pi^0\pi^0\eta$ data at 1.94GeV/c, two new $J^{PC}=2^{-+}$, isospin I=0 resonances are observed. A resonance with mass (1650±15) MeV and width (180±75) MeV is observed to decay into $a_2(1320)\pi^0$. The second new resonance has (1850±30) MeV mass with (225±75) MeV width and decays into $f_2(1270)\eta$. The resonance with 1650 MeV mass is a natural candidate for the η_2, the I=0 partner of the $\pi_2(1670)$. A third resonance with $J^{PC}=2^{++}$ is observed with a (2135±50) MeV mass and (250±50) MeV width; it is observed with decay modes into both $a_2(1320)\pi^0$ and $f_2(1270)\eta$. This third resonance is consistent with the $f_2(2170)$ claimed by GAMS. A tentative signal for a $J^{PC}=0^{-+}$ resonance with a (1625-1650) MeV mass decaying into $f_0(975)\eta$ is also observed.

Contents

Chapter 1

Introduction

This technical report has been produced by stripping the relevant information from Andy Cooper's thesis ("Analysis of $\bar{p}p \to \pi\pi\pi\eta$") in which $\pi^+\pi^-\pi^0\eta$ and $\pi^0\pi^0\pi^0\eta$ data were presented. Some references to the $\pi^+\pi^-\pi^0\eta$ data still remain but these should be ignored.

Mesons from the $J^P = 0^-$ nonet are called the *pseudoscalar mesons*. Other nonets include:-

- $J^P = 0^+$: Scalar mesons
- $J^P = 1^-$: Vector mesons
- $J^P = 1^+$: Axial-vector mesons
- $J^P = 2^-$: Pseudotensor mesons
- $J^P = 2^+$: Tensor mesons.

Some assignments of mesons to these nonets can be found in Table 1.1. As can be seen from Table 1.1, a large number of states remain unobserved. Some of the assignments, particularly in the 0^{++} multiplet, are controversial. The $f_0(975)$ and $a_0(980)$ are both candidates for $K\bar{K}$ molecules.[8] [9]

$N^{2S+1}L_J$	J^{PC}	$u\bar{d}$, $u\bar{u}$, $d\bar{d}$ I = 1	$u\bar{u}$, $d\bar{d}$, $s\bar{s}$ I = 0	$c\bar{c}$ I = 0	$b\bar{b}$ I = 0	$\bar{s}u$, $\bar{s}d$ I = 1/2	$c\bar{u}$, $c\bar{d}$ I = 1/2	$c\bar{s}$ I = 0	$\bar{b}u$, $\bar{b}d$ I = 1/2
$1\ ^1S_0$	0^{-+}	π	η,η'	η_c		K	D	D_s	B
$1\ ^3S_1$	1^{--}	ρ	ω,ϕ	$J/\psi(1S)$	$\Upsilon(1S)$	$K^*(892)$	$D^*(2010)$	$D_s^*(2110)$	$B^*(5330)$
$1\ ^1P_1$	1^{+-}	$b_1(1235)$	$h_1(1170)$,$h_1(1380)$			K_{1B}	$D_1(2420)$	$D_{s1}(2536)$	
$1\ ^3P_0$	0^{++}	$a_0(1450)$	$f_0(1335)$,$f_0(1590)$	$\chi_{c0}(1P)$	$\chi_{b0}(1P)$	$K_0^*(1430)$			
$1\ ^3P_1$	1^{++}	$a_1(1260)$	$f_1(1285)$,$f_1(1510)$	$\chi_{c1}(1P)$	$\chi_{b1}(1P)$	K_{1A}			
$1\ ^3P_2$	2^{++}	$a_2(1320)$	$f_2(1270)$, $f_2'(1525)$	$\chi_{c2}(1P)$	$\chi_{b2}(1P)$	$K_2^*(1430)$	$D_2^*(2460)$		
$1\ ^1D_2$	2^{-+}	$\pi_2(1670)$							
$1\ ^3D_1$	1^{--}	$\rho(1700)$	$\omega(1600)$	$\psi(3770)$		$K^*(1680)$			
$1\ ^3D_2$	2^{--}					$K_2(1770)$			
$1\ ^3D_3$	3^{--}	$\rho_3(1690)$	$\omega_3(1670)$, $\phi_3(1850)$			$K_3^*(1780)$			
$1\ ^3F_4$	4^{++}	$a_4(2040)$	$f_4(2050)$,$f_4(2220)$			$K_4^*(2045)$			
$2\ ^1S_0$	0^{-+}	$\pi(1300)$	$\eta(1295)$	$\eta_c(2S)$		$K(1460)$			
$2\ ^3S_1$	1^{--}	$\rho(1450)$	$\omega(1390)$,$\phi(1680)$	$\psi(2S)$	$\Upsilon(2S)$	$K^*(1410)$			
$2\ ^3P_2$	2^{++}		$f_2(1640)$		$\chi_{b2}(2P)$	$K_2^*(1980)$			
$3\ ^1S_0$	0^{-+}	$\pi(1770)$	$\eta(1760)$			$K(1830)$			

Table 1.1: Meson Table.

To compound the problems in searching for new mesons and filling nonets, exotic states have to be identified. It has been proposed[13] that some exotic states may have a spin-parity forbidden to $q\bar{q}$ eg $J^{PC} = 0^{--}$, 0^{+-}, 1^{-+} and 2^{+-}. However, no evidence for such states with abnormal J^{PC} has been found. Exotic states with acceptable $q\bar{q}$ spin-parity may be found by counting states. Once a nonet has been assigned nine resonances, a further state with the same quantum numbers provides evidence that one of the ten states is exotic. To identify which of the ten states does not fit in the nonet, the mass and relative strength of decay modes need to be studied. Reviews of the search for exotic states can be found in references [14],[15] and [16].

A model (based on spherical cavity approximation) used to predict glueball masses[17] agrees well with the current glueball candidates:-

- 0^- $\eta(1440)$ from Mark III data. [7]
- 0^+ $f_0(1500)$ from Crystal Barrel data. [18]
- 0 or 2^+ $\theta(1710)$ from Mark III and WA76 data. [19]

This model also predicts a $J^{PC} = 2^{-+}$ glueball with a mass in the region of 1700MeV. So far, no candidate for a 2^{-+} glueball has been observed.

The motivation for this analysis is to use $\bar{p}p \to \pi\pi\pi\eta$ Crystal Barrel data in order to observe some of the missing states, notably the I=0 $^1D_2$ state missing from Table 1.1. The observation of more than one 2^- state contributes to the search for the missing 2^- glueball candidate.

1.1 The Scope of this Analysis

In the following chapter, the $\bar{p}p \to \pi^0\pi^0\pi^0\eta$ at 1.94GeV/c data is presented. The qualitative features of the data are discussed there. Chapter 3 discusses a maximum likelihood fit to the data. These were chosen for the first analysis for two reasons.

Firstly a promising signal is visible by eye around $\eta\pi^0\pi^0$ masses of 1650MeV, where a 2^{-+} resonance is expected. Secondly, the isospin content of these data is simpler than $\pi^+\pi^-\pi^0\eta$, which contains a strong ρ signal and potentially I=1 $\eta\pi^\pm\pi^0$ resonances. This choice turned out to be a good one. Three definite resonances are located in the $\pi^0\pi^0\pi^0\eta$ data and a possible fourth. However, the analysis has been lengthy and complex. In the time available, it has not been possible to complete maximum likelihood analyses of the remaining three data sets. That remains a task for the future.

Chapter 2

Data Selection

2.1 Introduction

In order to analyse the $\pi\pi\pi\eta$ final state from antiproton-proton annihilation, the following data have been used:-

Run Period Date	$\bar{p}$ Momenta (Gev/c)	Trigger Type	Events Accumulated
July 92	1.94	0-Prong	1.469M

Table 2.1: Data Sets Used in Analysis.

In-flight data, as opposed to at-rest data, were used since they have the advantage of a larger range of phase space. The July 1992 data were the first large data set to be taken with an antiproton momentum of 1.94GeV/c.

2.2 Triggers Used in the Data Taking

The data used in this analysis were accumulated using the following trigger:-

- **0-Prong**: For an event to be accepted and written to tape, the event had to sequentially pass the following conditions:-
  - No signals (indicating a charged particle) from the PWCs or the JDC.
  - The number of FACE clusters must be greater than one.
  - The sum of the energy measured in the electromagnetic calorimeter must be within a suitable range defined within the software trigger.

2.3 Event Selection

The selection of $\bar{p}p \rightarrow \pi^0\pi^0\pi^0\eta$ events was done in several stages. From the raw data, the events were reconstructed, analysed and written to data summary tapes (DSTs) provided they passed the analysis cuts, *ie* the event fulfilled certain characteristics of being an $\pi^0\pi^0\pi^0\eta$ event. This process was repeated with increasingly sophisticated and constraining cuts (to produce DST$'$, DST$''$ etc) until the data samples contained only $\pi^0\pi^0\pi^0\eta$ events.

The electromagnetic split-off suppression package[33] uses the ratio of PED energies for 2-PED clusters to identify split-offs which are generally of low energy (< 50MeV). The opening angle between the two PEDs is used to avoid identifying PEDs from a fast π^0 as split-offs: photons from fast π^0s tend to have a small opening angle and are measured as two PEDs in the same cluster.

The measured parameters used in the kinematic fitting of photons are ϕ, θ and $\sqrt{\text{E}}$. These parameters were chosen since they are the least correlated and produce the most Gaussian-like error distribution. Similarly for charged particles the equivalent parameters are ψ, $\tan(\lambda)$ and $1/P_{xy}$ where λ is $(\pi/2$ - $\theta)$ and P_{xy} is the transverse momentum. For each attempted fit the package produces a *pull* for each parameter and a confidence level. The pull value is proportional to the difference between the measured and ideal parameter value. An example of a pull distribution can be seen in Figure 2.1.

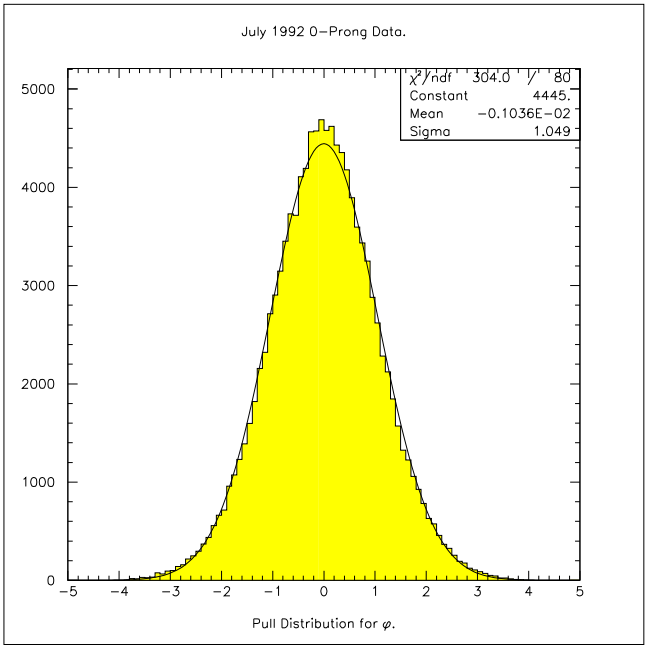

Figure 2.1: A typical pull distribution for the parameter ϕ fitted with a Gaussian distribution.

The mean and sigma, σ, of a pull distribution gives information about the magnitude and associated error for a particular parameter. The mean indicates whether the magnitude of the parameter measurement is, on average, too high or low. Likewise, σ indicates whether the errors have been underestimated or are too large. In an ideal situation where the measured parameters are independent, the data set is completely pure and the error magnitudes are known, the pull distributions for events with a confidence level greater than 0% should be Gaussian with a mean centered on zero and a σ equal to one. A distribution with a mean greater than zero indicates that the parameter has consistently been measured with a lower value than that of the real or ideal value. A mean less than zero indicates that the parameter measurement has been consistently too high. When the errors of a parameter are underestimated, the σ of the distribution is greater than one. A σ less than one indicates that the parameter errors are too large.

Using the confidence level and pull distributions, scaling factors for the parameters

and errors were used to ensure that the mean and σ for the pulls were close to zero and one respectively. For real data, the fit to $\pi^0\pi^0\pi^0\gamma\gamma$ was used to get the confidence level and pulls. This fit was used for the following reasons: the process $\bar{p}p \to \pi\pi\pi\gamma\gamma$ has a large branching ratio and so a small sample of data can be used to get large statistics. The events must have passed the energy-momentum fit to be included in the $\pi\pi\pi\gamma\gamma$ fit. The energy-momentum fit rejects most of the large number of events in which one or more particles went undetected. These events cause a bias in the pulls since they lower the mean energy of the events. The scaling factors used and the resulting confidence level and pull distributions for each kinematic fit can be found in Appendix A.

For the $\pi^+\pi^-\pi^0\eta$ final state, the charged pions were assumed to be stable and did not decay whilst in the detector. For both $\pi^+\pi^-\pi^0\eta$ and $\pi^0\pi^0\pi^0\eta$ final states the π^0 and η particles were identified by their decay into two photons. Therefore, assuming that no split-offs occurred or particles went undetected, the charged mode of $\pi\pi\pi\eta$ has an ideal final state of two charged pions and four photons. However, the process $\bar{p}p \to \pi^+\pi^-\pi^0\pi^0$ also has a final state of two charged pions and four photons and this has to be considered as a possible source of background when the four photons from $\pi^+\pi^-\pi^0\pi^0$ can be paired to form an η and π^0. The neutral mode of $\pi\pi\pi\eta$ has eight photons in its ideal final state. Other processes with an eight photon final state and hence possible sources of background are $\bar{p}p \to \pi^0\pi^0\pi^0\pi^0$ and $\bar{p}p \to \omega\omega\pi^0$ where both ω particles decay into $\pi^0\gamma$. To ensure the purity of the $\pi\pi\pi\eta$ data samples, events were rejected if they could be kinematically fitted to these background processes.

2.3.1 Analysis Cuts for $\bar{p}p \to \pi^0\pi^0\pi^0\eta$

In order to obtain a pure sample of $\bar{p}p \to \pi^0\pi^0\pi^0\eta$ events, the events read into the analysis software had to pass the following cuts. The reconstruction software used to do this was: CBOFF 1.22/00, LOCATER 1.52/04, BCTRAK 2.00/03, GTRACK 1.21/099 and CBKFIT 2.09/04.

- Cut1: The event must not have any charged tracks.
- Cut2: The event must have 8 unmatched PEDs.
- Cut3: Edge crystal (Type 13) cut.
- Cut4: The event must not have any electromagnetic split-offs. (DOLBY-C)
- Cut5: The event must fulfill a z-vertex fit with a confidence level greater than 0.0001%. The position of the $\bar{p}$ annihilation along the beam line, (z-axis), has a flat distribution along the target. Without the aid of charged tracks to point to a vertex, a kinematic fit is used to find the optimum position. The position of the vertex in the x-y plane is assumed to be at the centre of the target since the beam was steered to the centre of the target with high precision. This cut was deliberately loose since the fit was only used to find the best position of the vertex. A full energy-momentum fit with a more stringent confidence level cut is included in the next fit.
- Cut6: The event must fulfill a fit to the hypothesis $\pi^0\pi^0\pi^0\gamma\gamma$ with a confidence level greater than 1%.
- Cut7: The event must fulfill a fit to the hypothesis $\pi^0\pi^0\pi^0\eta$ with a confidence level greater than 1%.
- Cut8: The event must NOT fulfill a fit to the hypothesis $\pi^0\pi^0\pi^0\pi^0$ ie the confidence level must be less than 1%.
- Cut9: The event must NOT fulfill a fit to the hypothesis $\omega\omega\pi^0$ in which both ω particles decay into a $\pi^0\gamma$. For the event to be accepted, the confidence level from the fit must be less than 1%.

2.4 Monte Carlo Data

Monte Carlo data have been generated and used to give an approximate simulation of the phase space for the pions and η in the $\pi\pi\pi\eta$ final state. The data were generated using a CERN software package; GEANT 3.15 and GCB 4.06/07, and analysed using identical reconstruction and analysis software as that for the real data. By comparing the kinematics of the generated $\pi\pi\pi\eta$ particles with the same reconstructed data set, the geometric effects of the detector and the reconstruction efficiency can be evaluated.

The vertex of the annihilation was generated with a gaussian distribution with a 2cm sigma to simulate the distribution of real in-flight annihilations within the liquid hydrogen target. Since the annihilations occurred in-flight, the resulting particles are boosted along the beam axis and angular momentum effects may also bias the particles along the beam line direction. The latter effect was not included in the simulation since there are a large number of possible initial states in this energy region. The decays of the η and π^0 were not left free; both particles were forced to decay via two photons 100% of the time.

Table 2.2 shows the number of events generated for the various data sets.

Monte Carlo Data Set	$\bar{p}$ Momenta (Gev/c)	Events Accumulated
MC $\bar{p}p \rightarrow \pi^0\pi^0\pi^0\eta$	1.94	95K
MC $\bar{p}p \rightarrow \pi^0\pi^0\pi^0\pi^0$	1.94	95K

Table 2.2: Monte Carlo data sets generated.

2.5 Selection Efficiency

Tables 2.3 show the loss of events for real and Monte Carlo data as they pass through the analysis. The number of lost events is given in terms of the percentage of events that failed a particular cut, relative to the number of events going into the cut.

Selection of $\bar{p}p \to \pi^0\pi^0\pi^0\eta$ at 1.94GeV/c				
	Real Data		MC Data	
Number of Events Analysed	1 469 109		95 419	
Cut	Passed	Lost(%)	Passed	Lost(%)
No Charged particles	1 127 552	23.3	87 401	8.4
8 Unmatched PEDs	198 223	82.4	38 331	56.1
No Edge Crystal PEDs	101 544	48.8	22 543	41.2
No EM split-offs	87 923	13.4	20 336	9.8
CBKFIT: Z-Vertex Fit CL $> 1\times10^{-4}$%	57 546	34.6	17 029	16.3
CBKFIT: Fit to $3\pi^0\gamma\gamma$ CL > 1%	47 168	18.0	14 642	14.0
CBKFIT: Fit to $3\pi^0\eta$ CL > 1%	11 076	76.5	13 407	8.4
CBKFIT: No fit to $4\pi^0$ CL < 1%	7 598	31.4	13 212	1.5
CBKFIT: No fit to $\omega\omega\pi^0$ CL < 1%	6 933	8.8	11 864	10.2

Table 2.3: Loss of events as they pass through the analysis cuts for events of the form $\bar{p}p \to \pi^0\pi^0\pi^0\eta$ with a $\bar{p}$ momentum of 1.94GeV/c. The real data is from the 0-prong trigger data of July 1992.

2.6 Background Channels

After the fit to $\pi\pi\pi\gamma\gamma$ the invariant mass of the remaining photon pair was calculated. The resulting invariant mass plots for each data set can be seen in Figure

2.2. These show clearly that the relative branching ratio for 4π and $3\pi\eta$ produced in proton-antiproton annihilation is different for the charged and neutral channels but are not sensitive to the change in energy.

Estimating that the relative branching ratio, (R), for $\bar{p}p \to \pi\pi\pi\pi$ to $\bar{p}p \to \pi\pi\pi\eta$ is 5:1 for the neutral data at both energies, then the amount of the $\pi\pi\pi\pi$ background channel can be calculated using equation 2.1.

$$\%Background = \frac{R \times \varepsilon(\pi\pi\pi\pi) \times 100\%}{1 \times \varepsilon(\pi\pi\pi\eta)} \tag{2.1}$$

The efficiencies $\varepsilon(\pi\pi\pi\eta)$ and $\varepsilon(\pi\pi\pi\pi)$ for events passing through the $\pi\pi\pi\eta$ analysis cuts have been calculated using Monte Carlo data for three different confidence level cuts for the fit to $\pi\pi\pi\eta$. These efficiencies and the corresponding percentage background can be found in Tables 2.4.

Background to $\bar{p}p \to \pi^0\pi^0\pi^0\eta$ at 1.94GeV/c			
Fit to $\pi^0\pi^0\pi^0\eta$	$\varepsilon(\pi^0\pi^0\pi^0\eta)$	$\varepsilon(\pi^0\pi^0\pi^0\pi^0)$	Background
CL Cut: $> 1\%$	12.43	0.28	11%
CL Cut: $> 10\%$	9.72	0.12	6%
CL Cut: $> 20\%$	8.18	0.08	5%

Table 2.4: Background for $\pi^0\pi^0\pi^0\eta$ at 1.94GeV/c.

The few 4π events that do manage to pass through the $\pi\pi\pi\eta$ cuts, despite the veto, have a flat distribution in the $\pi\pi$ versus $\pi\eta$ scatter plots for a 10% confidence level cut on the fit to $\pi\pi\pi\eta$. This is seen for all four data sets (as a typical example, see Figure 2.3) and therefore it is assumed that the 4π channel contributes a structureless background to the $\pi\pi\pi\eta$ data.

The invariant mass distribution for the remaining photon pair, after background channel cuts, can be found in Figure 2.4. Events successfully fitted to $\bar{p}p \to \pi\pi\pi\pi$, (and in addition, $\omega\omega\pi$ for the all-neutral data) were not included in the latter figure.

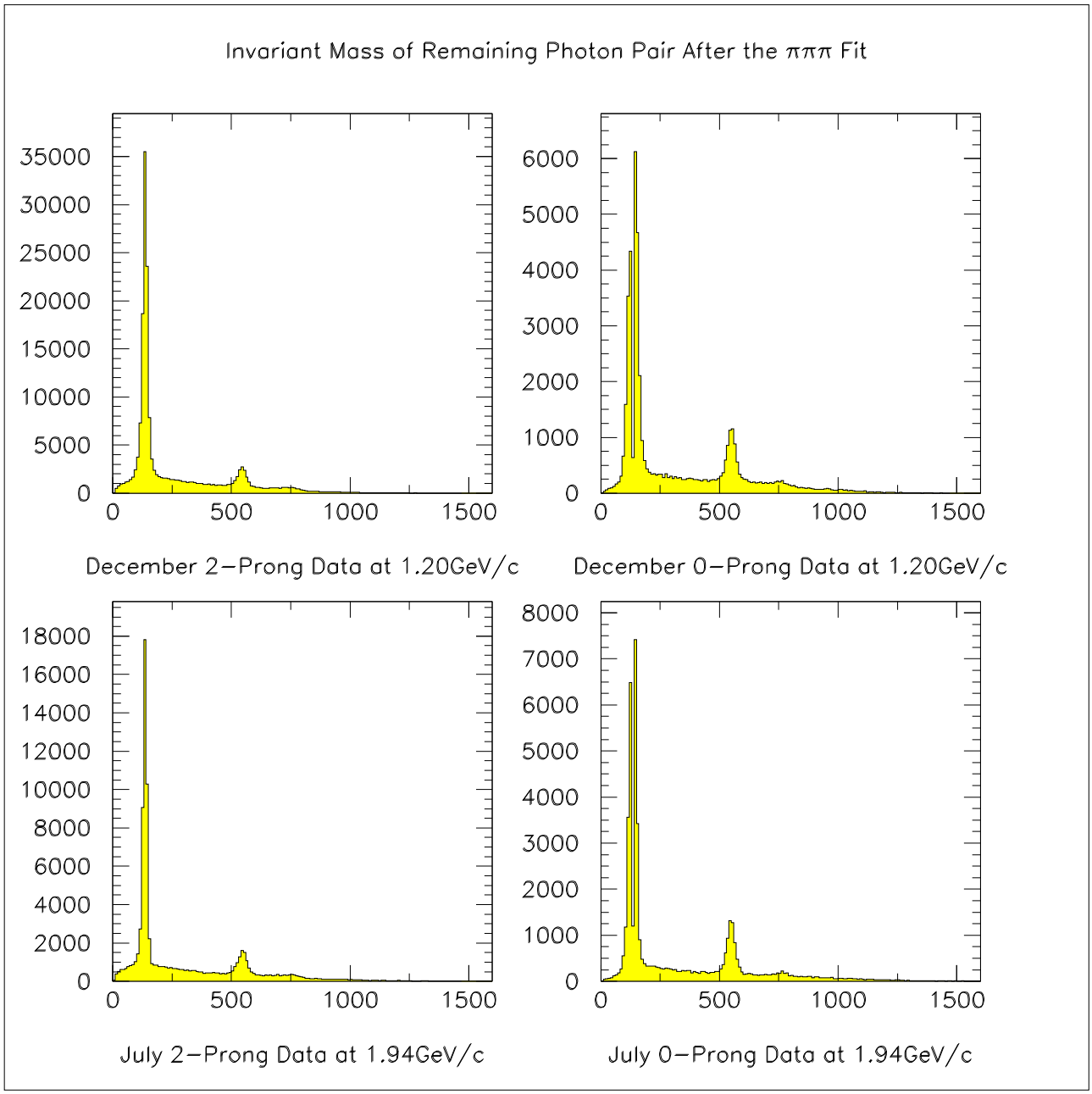

Figure 2.2: Invariant mass plots of the remaining photon pair after a fit to three pions. The two clear peaks are the π^0 and η from $\pi\pi\pi\pi$ and $\pi\pi\pi\eta$ events. The hole in the π^0 peak of the 0-prong data is due to the peak corresponding to the worst measured π^0 of the four π^0s; the best three have already been selected in the fit to $\pi^0\pi^0\pi^0\gamma\gamma$ and removed to leave the remaining photon pair.

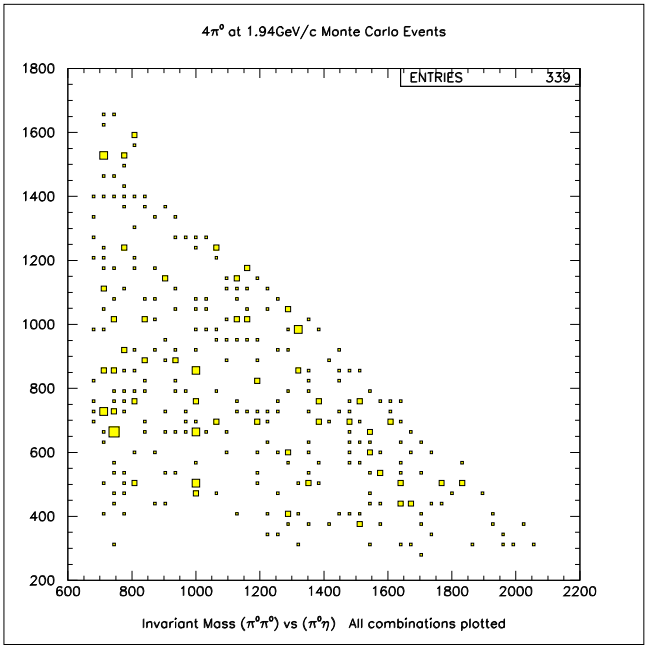

Figure 2.3: Scatter plot for $4\pi^0$ Monte Carlo events that passed the $\pi^0\pi^0\pi^0\eta$ event selection cuts.

The η peaks now show a good signal to noise ratio. The remaining background under the η peaks is due to the kinematic fitting package wrongly pairing photons and also the incomplete kinematic reconstruction of channels with a similar final state.
To avoid the four pion background channels a 10% confidence level cut was used for the kinematic fits to $\pi\pi\pi\eta$ when creating the final data sets used for this analysis.

2.7 Mass Resolution

An estimate of the detector's mass resolution has been made using photons produced in the decay of the π^0 and η particles. By calculating and plotting (Figure 2.5 Top) the invariant mass of all unmatched PED pair combinations, a π^0 peak can be seen. An η peak can be seen (Figure 2.5 Bottom) when the unmatched PEDs that can form an invariant mass in the π^0 mass region are ignored. These invariant mass plots were produced after the following cuts were made:-

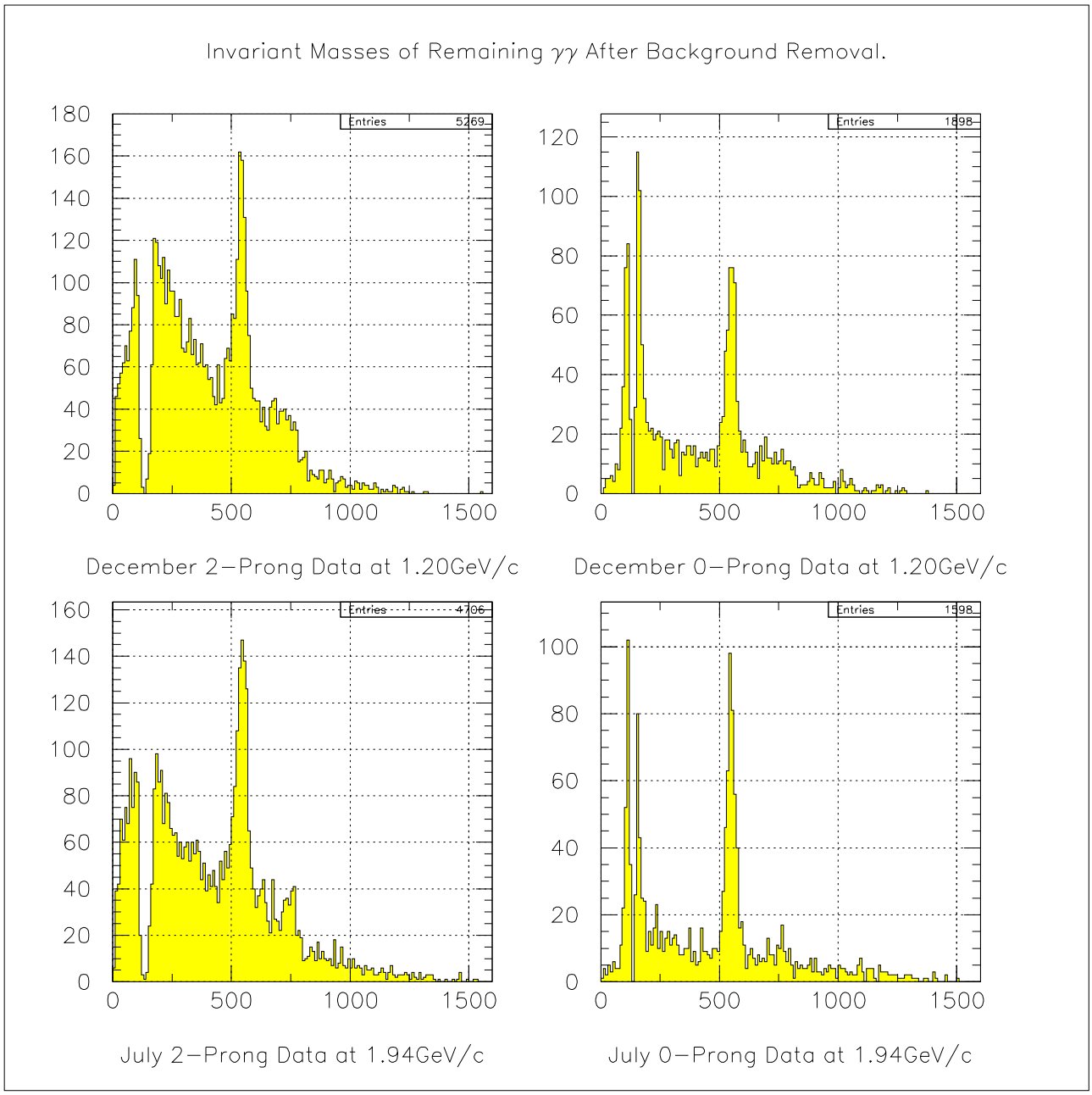

Figure 2.4: Invariant mass of the remaining photon pair after events successfully fitted to background channels have been removed.

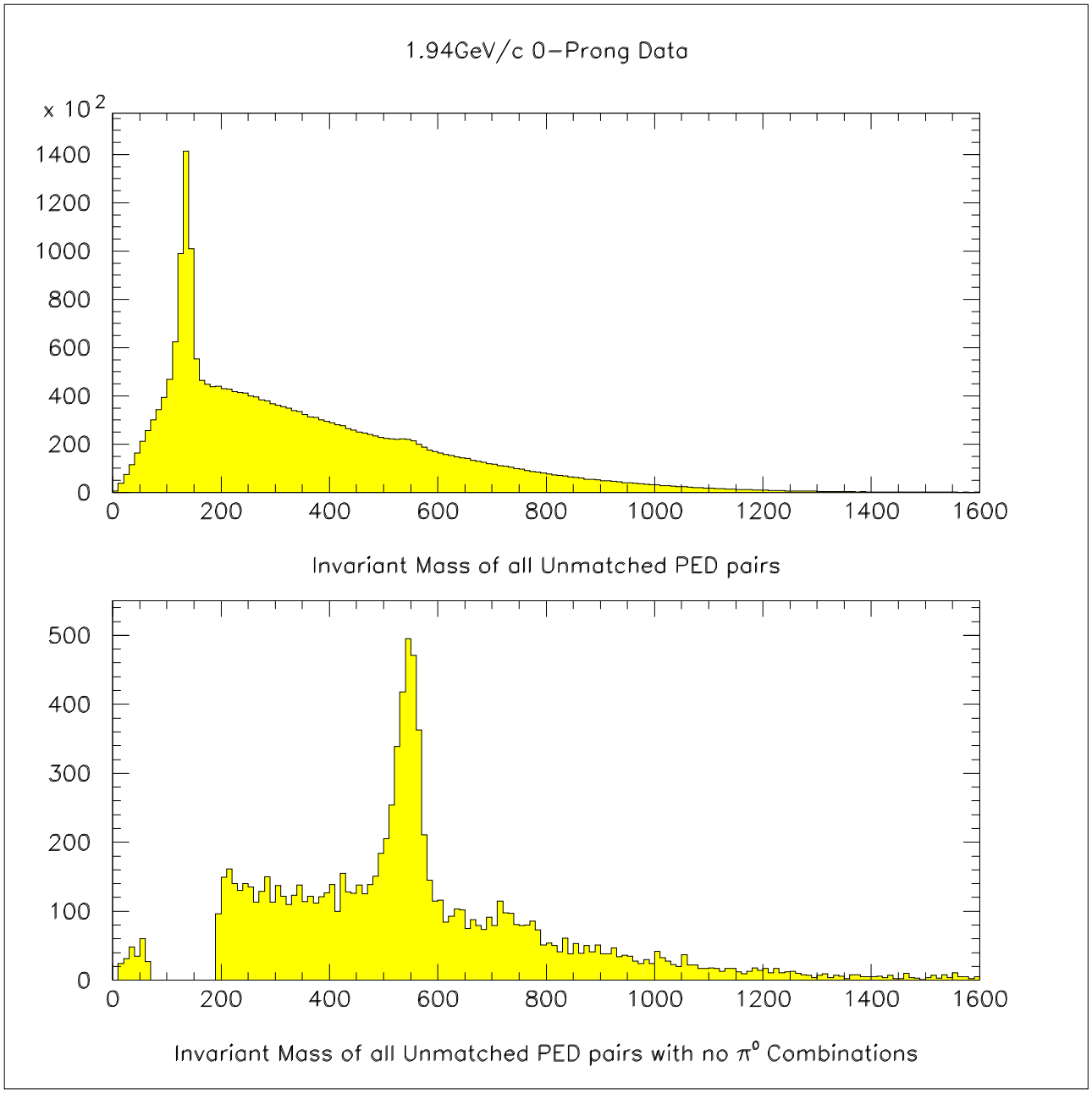

Figure 2.5: Top: Invariant mass of unmatched PED pairs. All combinations are plotted. Bottom: Invariant mass of unmatched PED pairs. All combinations not involved in the π^0 mass region are plotted.

- Charged data.
  - Two charged tracks of equal and opposite sign.
  - 3 < Number of unmatched PEDs > 7.
  - No events with an edge-crystal PED.
- All-neutral data.
  - Eight unmatched PEDs, No charged tracks.
  - No events with an edge-crystal PED.
  - No events with electromagnetic split-offs.

The π^0 and η peaks have been fitted with a Gaussian distribution with the background fitted using a 4^{th} order polynomial. The results from the fits can be seen in Tables 2.5 and 2.6.

Data Set	Momentum	m(π^0) MeV	$\sigma(\pi^0)$ MeV	Resolution
0-Prong	1.94	134.95 ± 0.02	9.71 ± 0.03	7.20%

Table 2.5: Mass resolutions calculated using π^0 peaks.

Data Set	Momentum	m(η) MeV	$\sigma(\eta)$ MeV	Resolution
0-Prong	1.94	544.5 ± 0.8	20.7 ± 0.8	3.8%

Table 2.6: Mass resolutions calculated using η peaks.

All four different data sets show that the detector has a very good mass resolution and that the fractional energy resolution (ΔE/E) and the position resolution improve with increasing photon energy. This can be explained by the high energy photons producing large showers which have less significant statistical fluctuations and span many crystals.

2.8 Summary of Data Selection

Over 10 million raw data events (9327K of real data and 956K of Monte Carlo data) have been accumulated and processed. Table 2.7 summarizes the data sets used and the fraction of events that passed the standard selection criteria for $\pi^+\pi^-\pi^0\eta$ and $\pi^0\pi^0\pi^0\eta$ events.

Data Set	$\bar{p}$ Momenta (Gev/c)	Events Analysed	Events Passed	Events Passed (%)
Real: Jul 92 0-Prong	1.94	1 469K	6 993	0.47
MC $\bar{p}p \to \pi^0\pi^0\pi^0\eta$	1.94	95K	11 864	12.43
MC $\bar{p}p \to \pi^0\pi^0\pi^0\pi^0$	1.94	95K	267	0.28

Table 2.7: Data Sets Used in the Analysis.

The most likely source of background to the $\pi^+\pi^-\pi^0\eta$ data comes from $\pi^+\pi^-\pi^0\pi^0$ events. The $\pi^0\pi^0\pi^0\eta$ data has two channels that may contribute to background: $\pi^0\pi^0\pi^0\pi^0$ and $\omega\omega\pi^0$. All background channels are fitted and events rejected if the resulting confidence level is greater than 1%. Contamination due to the $\omega\omega\pi^0$ channel is thought to be negligible due to it's low branching ratio. Those 4π events that do filter through the analysis cuts do not produce a structured background. To reduce the background channel contamination further, a confidence level of 10% for the fit to $\pi\pi\pi\eta$ was used.

Chapter 3

Mass Distributions

3.1 Introduction

This chapter presents the general invariant mass distributions for the $\pi^0\pi^0\pi^0\eta$ data. The plots have the following conventions: real data distributions are shown with error bars whilst the acceptance corrected phase space Monte Carlo data are given by solid lines; The real data are normalized to one and Monte Carlo are arbitrarily normalized so that the Monte Carlo profiles match the real data profiles in *non-resonant* mass regions. The Monte Carlo data have been smoothed using a smoothing algorithm[36] to reduce any statistical fluctuations.
The data sets contain a dominant and well understood process:-

- **0-Prong**: $\bar{p}p \to \eta\eta_{(3\pi)} \quad (\eta_{(3\pi)} \to \pi^0\pi^0\pi^0)$ Figure 3.1

The $\bar{p}p \to \eta\eta$ events are of little interest in this analysis and are not included in the mass plots. The events are easily and safely removed (by using a kinematic fit with a confidence level cut of 1%) since they involve narrow states and have a high signal to background ratio. The number of remaining events left after the $\eta\eta$ events have been removed can be found in Table 3.1.

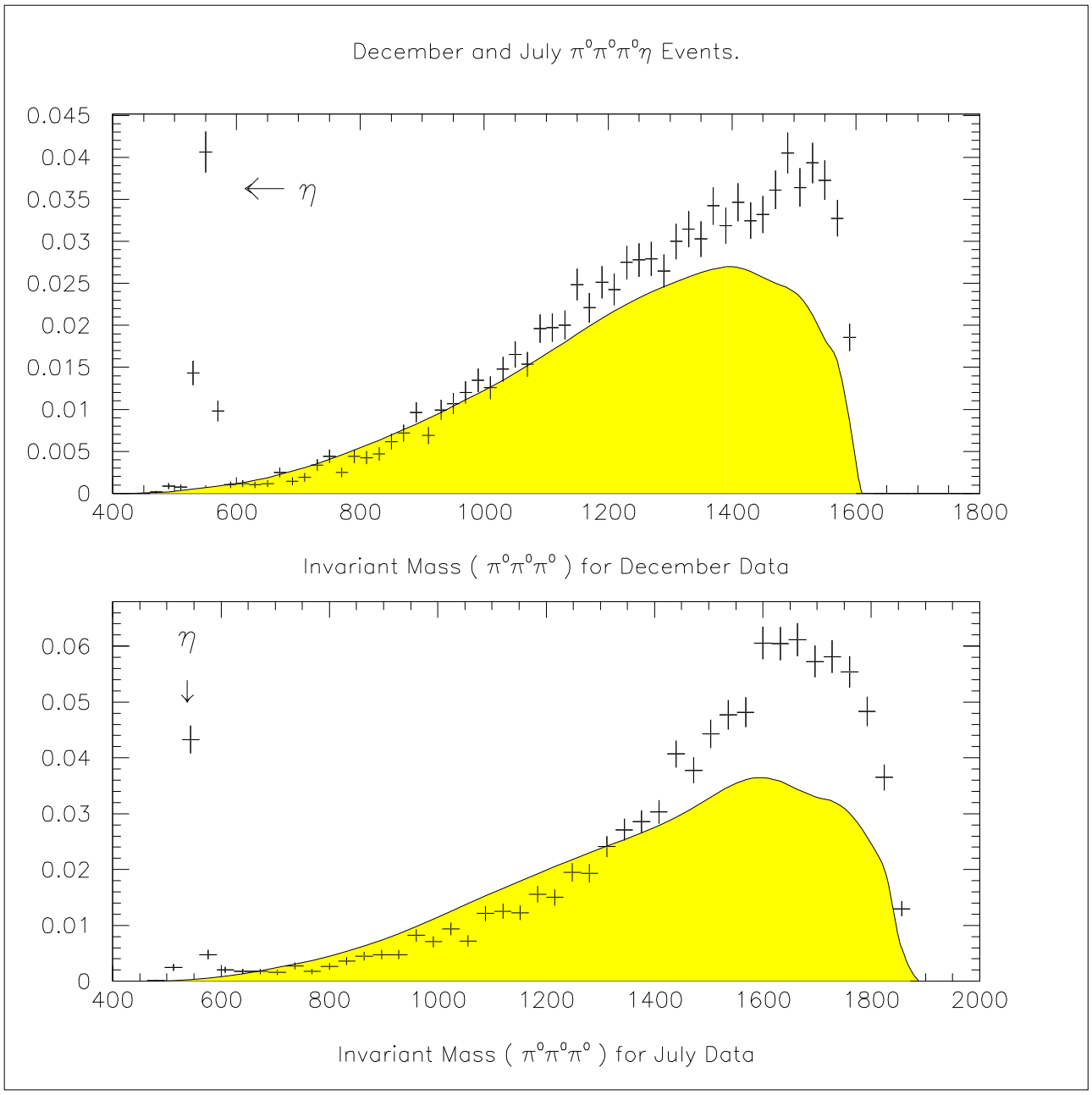

Figure 3.1: $\pi^0\pi^0\pi^0\eta$ at 1.20GeV/c (December 1991) and 1.94GeV/c (July 1992). Both data sets show signals for the η corresponding to $\bar{p}p \to \eta\eta$ events. The shaded mass distribution represents the Monte Carlo data.

Data Set	$\bar{p}$ Momentum (GeV/c)	Events	MC Events
$\pi^0\pi^0\pi^0\eta$	1.94	4 627	9 265

Table 3.1: Event numbers for each data set used in this analysis.

3.1.1 $\pi^0\pi^0\pi^0\eta$ at 1.94 GeV/c

Mass plots for $\bar{p}p \to \pi^0\pi^0\pi^0\eta$ at 1.94 GeV/c (Figures 3.2 to 3.4) present the following invariant mass distributions:

- Invariant Mass $(\pi^0\pi^0\pi^0)$
- Invariant Mass $(\pi^0\pi^0\eta)$
- Invariant Mass $(\pi^0\eta)$
- Invariant Mass $(\pi^0\pi^0$ v. $\pi^0\eta)$ - All 6 combinations plotted.

The prominent channels in the data are:-

- $\bar{p}p \to a_0(980)f_2(1270) \to (\pi^0\eta)(\pi^0\pi^0)$
- $\bar{p}p \to a_2(1320)\sigma \to (\pi^0\eta)(\pi^0\pi^0)$.

Peaks in the $(\pi^0\pi^0\eta)$ mass distribution show the $\eta'(958)$ and $f_1(1285)$ in the channels:-

- $\bar{p}p \to \pi^0 f_1(1285) \to \pi^0(\pi^0\pi^0\eta)$
- $\bar{p}p \to \pi^0 f_1(1285) \to \pi^0[a_0(980)\pi^0] \to \pi^0(\pi^0\eta)\pi^0$.

A discrepancy between the real and Monte Carlo data can be seen in the $(\pi^0\pi^0\eta)$ (1500-1900)MeV mass region and also in the $(\pi^0\pi^0\pi^0)$ (1500-1900)MeV mass region. A possible source of the latter enhancement is the $\pi_2(1670)$ in:-

- $\bar{p}p \rightarrow \eta\pi_2(1670) \rightarrow \eta[\pi^0 f_2(1270)] \rightarrow \eta\pi^0(\pi^0\pi^0)$.

No well established mesons with broad widths and a decay mode into $(\pi^0\pi^0\eta)$ can account for the enhancement in the $(\pi^0\pi^0\eta)$ mass distribution.

3.1.2 Comparison of $\bar{p}p \rightarrow \pi^0\pi^0\pi^0\eta$ at 1.20 and 1.94 GeV/c

As for the charged data, the increase in phase space produces a large $a_0(980)f_2(1270)$ signal in the 1.94GeV/c data. The higher energy data set exhibits a strong enhancement in the $(\pi^0\pi^0\eta)$ (1500-1900)MeV mass region not evident in the 1.20GeV/c data set. This may be attributed to several possibilities: (a) The strong $a_0(980)f_2(1270)$ and/or $\eta\pi_2(1670)$ signal(s) contributes a considerable phase space distortion, thus the $(\pi^0\pi^0\eta)$ enhancement may be a reflection. (b) The increased strength of the $a_2(1320)\sigma$ signal may be the source of the enhancement. (c) The enhancement may be due to one or more resonances decaying into $(\pi^0\pi^0\eta)$.

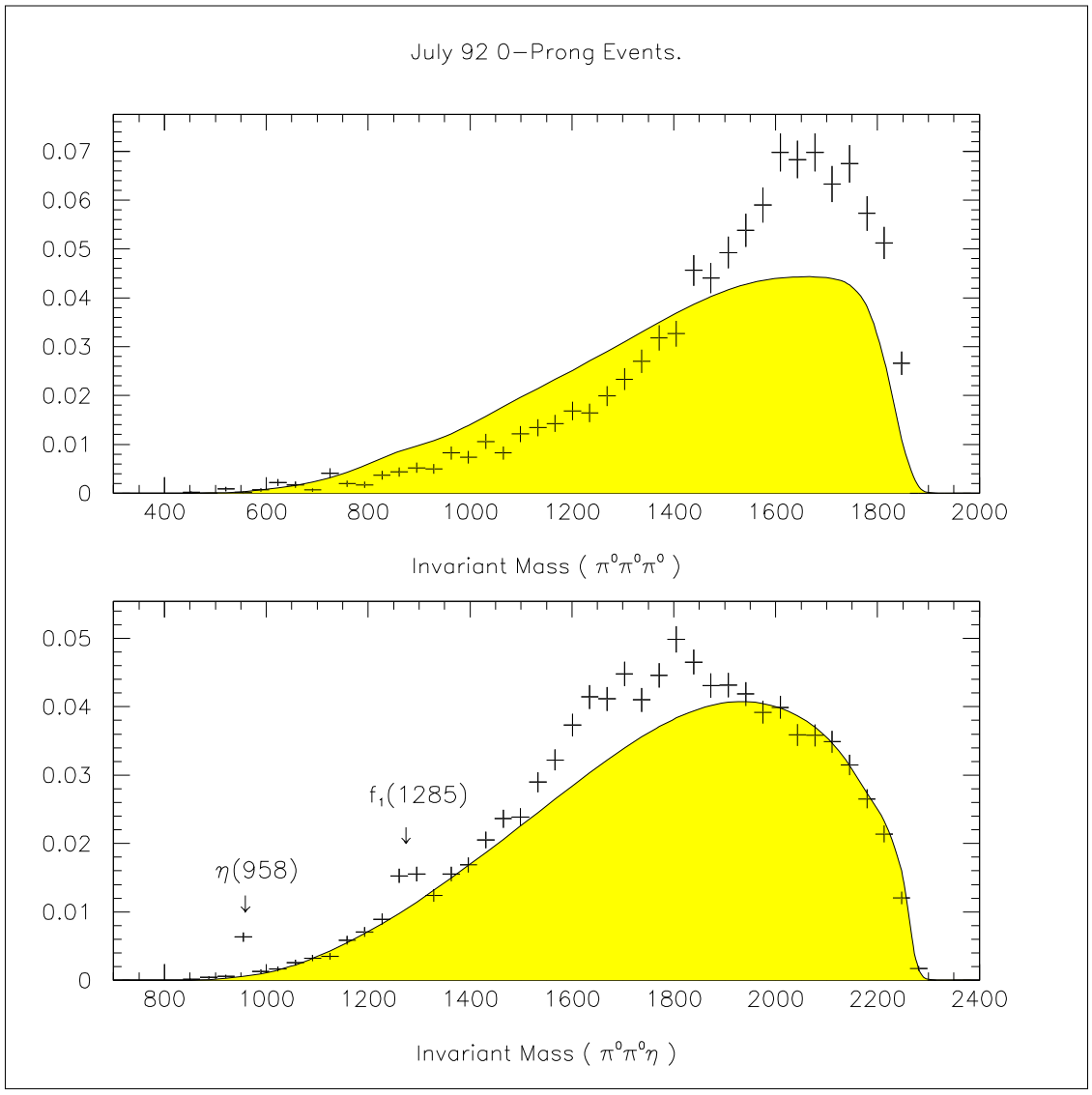

Figure 3.2: 1.94GeV/c data. Top: Invariant Mass of $(\pi^0\pi^0\pi^0)$. The MC and real data greatly differ above 1500 MeV. Bottom: Invariant Mass of $(\pi^0\pi^0\eta)$. Peaks due to the $\eta'(958)$ and $f_1(1285)$ are seen. A large discrepancy occurs between 1500 and 1900 MeV.

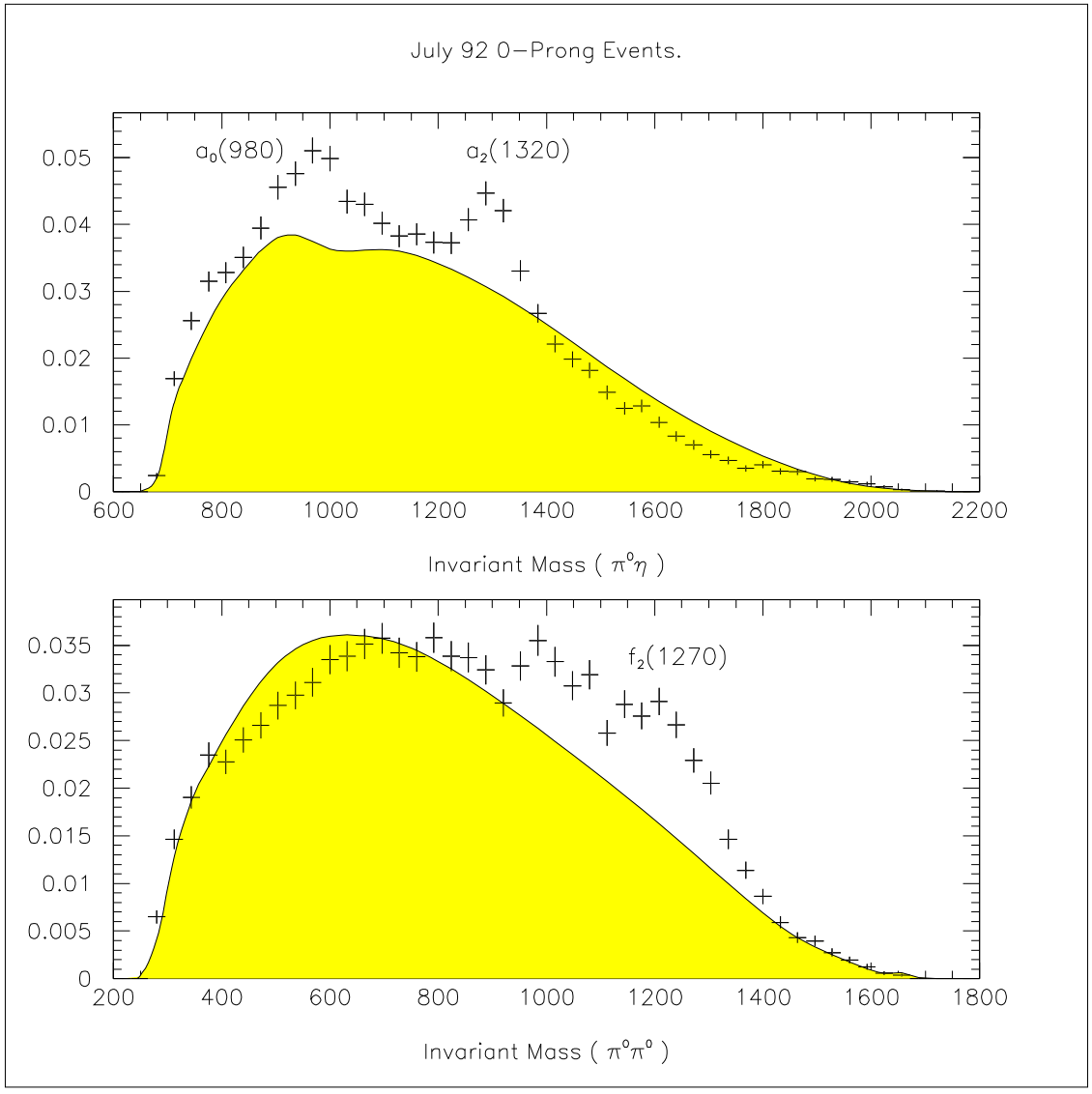

Figure 3.3: 1.94GeV/c data.Top: Invariant Mass of $(\pi^0\eta)$. Peaks due to the $a_0(980)$ and $a_2(1320)$ are seen. Bottom: Invariant Mass of $(\pi^0\pi^0)$ showing a signal for the $f_2(1270)$.

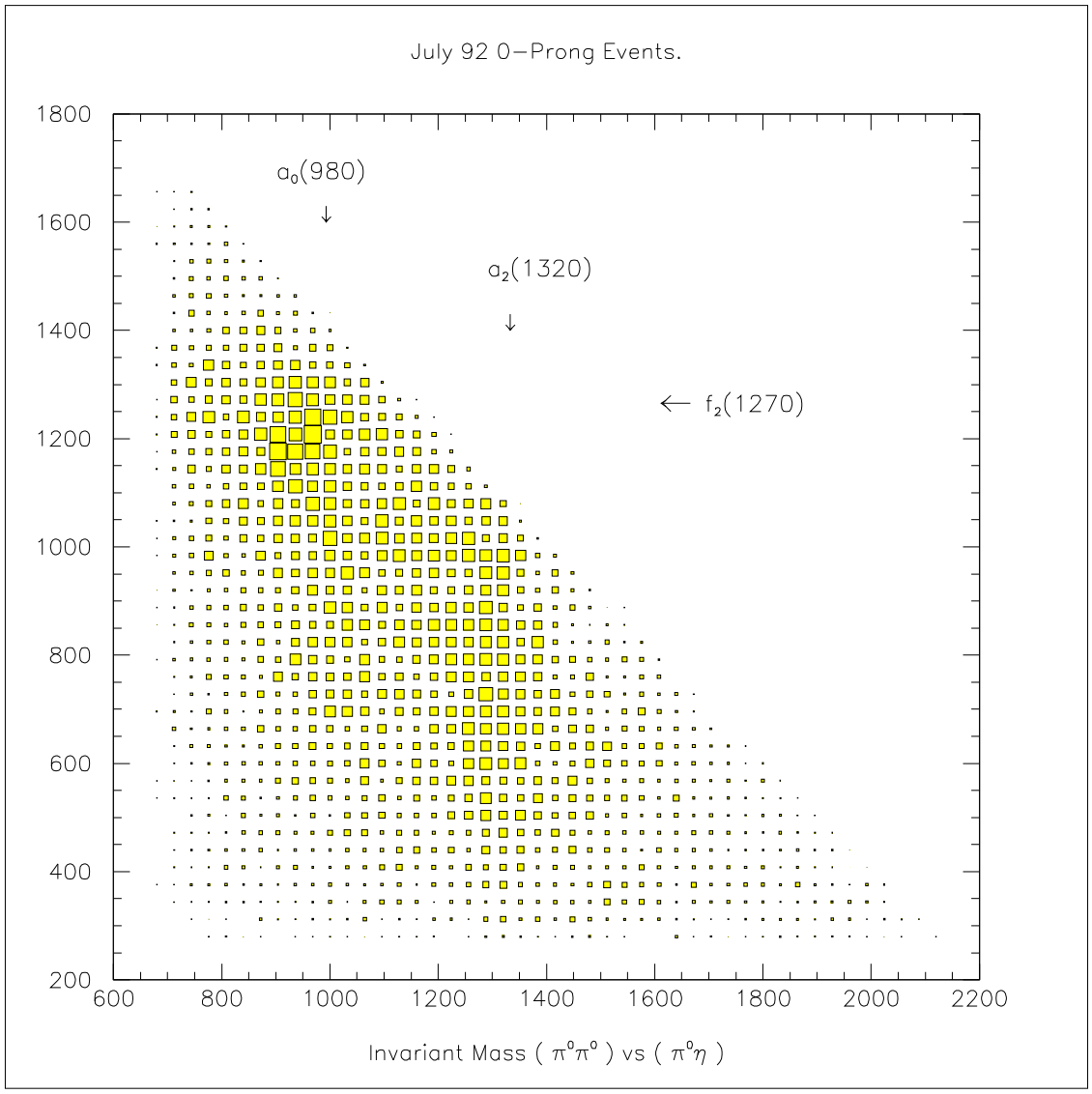

Figure 3.4: 1.94GeV/c data. Invariant Mass of $(\pi_i^0\pi_j^0)$ versus $(\pi_k^0\eta)$ showing the $a_0(980)$ and $a_2(1320)$ bands. A strong signal for $a_0(980)f_2(1270)$ events is seen. Six combinations of i, j and k are summed in this plot.

3.2 Summary

The narrow peaks in the invariant mass distributions showing the $\eta\eta$ channels in Figure 3.1 illustrate the good mass resolution of the data. Events successfully fitted to this channel are removed since they are of no interest in this analysis.
The neutral data shows strong signals in the channels:-

- $\bar{p}p \rightarrow a_2(1320)\sigma$
- $\bar{p}p \rightarrow a_0(980)\sigma$
- $\bar{p}p \rightarrow a_0(980)f_2(1270)$.

The charged data has evidence suggestive of a resonance with mass between (1600-1800)MeV that decays into all charge combinations of $\eta\rho$. The 1.94GeV/c all neutral data has a large enhancement in the (1500-1900)MeV ($\pi^0\pi^0\eta$) mass region. Both features are very interesting prospects for the 2^- pseudotensor mesons but the all neutral data enhancement was chosen for particular attention because of the simplified spin analysis: the charged data is more complex since it contains isospin I=1 resonances.
The following chapter presents the spin analysis of the $\pi^0\pi^0\pi^0\eta$ data at 1.94GeV/c and demonstrates that the ($\pi^0\pi^0\eta$) enhancement is due to two $J^{PC}=2^{-+}$ states.

Chapter 4

Spin Analysis

4.1 Maximum Likelihood Method

The $\bar{p}p \to \pi^0\pi^0\pi^0\eta$ 1.94GeV/c data were fitted using the maximum likelihood minimisation method[40]. The fitting package allows up to 100 parameters (70 may be free) and returns the negative log likelihood, s, given by equations 4.1 and 4.2.

$$s = \sum_{i=1}^{M} -\ln Y_i \tag{4.1}$$

$$Y_i = \frac{\mid f_A(x_i,\Theta) + f_B(x_i,\Theta) \mid^2}{\sum_{j=1}^{N} \mid f_A(x_j,\Theta) + f_B(x_j,\Theta) \mid^2} \tag{4.2}$$

Here, the indices i and j sum over the total number of real and Monte Carlo data events respectively. In this example, f_A and f_B represent the amplitudes of two channels. The measured quantities $\mathbf{x}$ are masses (like m($\pi^0\eta$), m($\pi^0\pi^0$), m($\pi^0\pi^0\eta$) etc) and various angles to describe the decay of $a_2(1320)$, $f_2(1270)$ etc. The strength of the amplitudes are dependent on the mass and width of resonances involved in the channel. These parameters are included in the term Θ. If the mass and width of resonances involved in the fit are fixed, then the free parameters can be reduced to channel coupling strengths, momentum transfer and interference terms.

The zero point for the scale of s is arbitrary and therefore it is the change in s that

is used to determine whether a channel contributes to the data. For this analysis, a significant improvement to a fit was implied by a *reduction* in the value of s, namely by at least 20.

4.2 Basic Fit to $\bar{p}p \to \pi^0\pi^0\pi^0\eta$

To outline the spin analysis procedure, the process

$$\bar{p}p \to \mathrm{X}\pi^0 \to [a_2(1320)\pi^0]\pi^0 \to (\eta\pi^0)\pi^0\pi^0$$

is used as an illustration. An arbitrary J^P for particle X is allowed. Since the data were in-flight, many initial angular momentum states of the antiproton and proton system are possible. No attempt to include a rigorous representation of the production process is made in the fit. Instead, it is assumed that X is produced with helicity, λ, along the beam direction, and the density of states is described by a density matrix, $\rho(\lambda\lambda')$ which is averaged over all production angles of X. The decay of X is analysed in full.

Suppose X is produced at angles (θ,ϕ) to the beam (with the z-axis along the beam direction). These angles are determined from the kinematics of the event for all six combinations of $(\eta\pi_i^0)\pi_j^0$. Suppose the production amplitude for helicity λ is f_λ^X. If the axes are rotated such that the new z-axis lies in the direction of X, the amplitude is multiplied by a D matrix, $\mathrm{D}^J_{\lambda\lambda'}(\theta,\phi)$. The amplitude is then invariant[41] under a Lorentz boost to the rest frame of X. However, the D matrix can be removed by rotating the axes back through angles (-θ,-ϕ) in the rest frame of X. This process is the Wick rotation, (described in reference [41]), between the laboratory frame and rest frame of X.

If the particle X decays to $a_2(1320)\pi^0$, the decay process can be described in the usual way using Clebsch-Gordan coefficients:

$$f_\lambda = (J,\lambda \mid L,m,2,\lambda-m)P_L^m(\gamma,\epsilon) \mid 2,\lambda-m > \qquad (4.3)$$

where γ and ϵ are the angles for $a_2(1320)$ with respect to the beam direction in the rest frame of X. The decay X $\rightarrow a_2(1320)\pi^0$ may now be treated as in the previous paragraph, with a second Wick rotation to the rest frame of $a_2(1320)$. Finally, the decay $a_2(1320) \rightarrow \eta\pi^0$ is described by Legendre polynomials $P_2^{\lambda-m}(\alpha,\beta)$, where (α,β) are the angles of η with respect to the beam direction in the rest frame of $a_2(1320)$. The result of this procedure is the following expression:

$$f_\lambda = (J, \lambda \mid L, m, 2, \lambda - m) P_L^m(\gamma, \epsilon) P_2^{\lambda-m}(\alpha, \beta) \tag{4.4}$$

where Wick rotations are included in (γ,ϵ) and (α,β). The initial $\bar{p}p$ state can have at most helicity λ=1. Therefore, channels with λ=2 contain an additional sinθ term due to one unit of orbital angular momentum in the final state. Helicity 3 was tried where necessary but rejected due to it's negligible contribution to the fit.

Interference amongst all channels with the same helicity were included in the fit. For interference between two channels, the interference terms were retained if the interference improved the fit by more than Δs=-10. The interference will be complete only if the initial state is the same for both channels. Since there are many possible initial states, the interference was constrained to lie within the range 0 (no coherence) to 1 (full coherence). Interference amongst channels with different values of helicity were not included in the fit due to their negligible contribution.

The only attempt to model the production process was the inclusion of a factor to describe the production angular distribution:

$$e^{\alpha\tau^2} \quad where \quad \tau = 2p_1p_2cos(\theta) \tag{4.5}$$

Here p_1 and p_2 are the centre of mass momenta of the initial antiproton and X.

The Wick rotation procedure is equivalent to using D matrices but has the advantage that it is faster to compute once the geometrical rotations have been calculated for any individual event. Also, the information concerning the initial helicity is preserved: for X(J^{PC}=2^{-+}) $\rightarrow a_2(1320)\pi^0$, where L=0, the helicity of X is transferred

directly to the $a_2(1320) \to \eta\pi^0$ decay. Typically, a fit takes less than one minute of real time to converge.

4.2.1 The Basic Fit Ingredients

The first fit included the obvious channels:

$$\bar{p}p \to \mathrm{f}_2(1270).a_0(980) \to (\pi^0\pi^0)(\pi^0\eta) \qquad \text{Channel 1}$$

$$\bar{p}p \to \sigma.a_2(1320) \to (\pi^0\pi^0)(\pi^0\eta) \qquad \text{Channel 2}$$

resulting in a log likelihood of s=326. The σ represents the $\pi^0\pi^0$ S-wave amplitude. The parameterisation of the $\pi^0\pi^0$ S-wave amplitude can be found in reference [39]. When one of the two channels is removed from the fit, the remaining channel's coupling strengths show little variation: evidence that the two channels are only slightly correlated and that interference between the two channels is negligible.
Further channels were included in the fit:

$$\bar{p}p \to \pi^0 f_1(1285) \to \pi^0[\pi^0 a_0(980)] \to \pi^0\pi^0(\pi^0\eta) \qquad \text{Channel 3}$$

$$\bar{p}p \to \sigma.a_0(980) \to (\pi^0\pi^0)(\pi^0\eta) \qquad \text{Channel 4}$$

and improve the log likelihood by Δs=-70 and Δs=-185 respectively. The removal of channel 3 from the fit increases the log likelihood by only Δs=+39. This suggests that channel 4 compensates to some extent for the removal of channel 3. The magnitude of the change in log likelihood gives an idea of the sensitivity of the fit; The $f_1(1285)$ peak is narrow and clearly seen by eye in Figure 3.2 (and later in Figure 4.9) and therefore may be considered as a highly significant signal.
A comparison of the real data and Monte Carlo data biased by the fit parameters, (Figure 4.1), shows a discrepancy in the $\pi^0\eta$ mass projection. The real data contains a broad enhancement in the mass region between the $a_0(980)$ and $a_2(1320)$ peaks. To remove this difference it was found necessary to include a term that describes an

incoherent phase space background in the real data. Monte Carlo simulations show that all of the resonances expected around 1700MeV and 2000-2100MeV in $\eta\pi\pi$ tend to give $(\eta\pi)$ combinations with a broad peak from 1000-1500MeV. The background term may be due to these resonances, presently invisible. Whatever it's origin, this background term gave a large improvement to the fit, Δs=-327. However, it plays no role in the identification of the resonances now to be discussed.

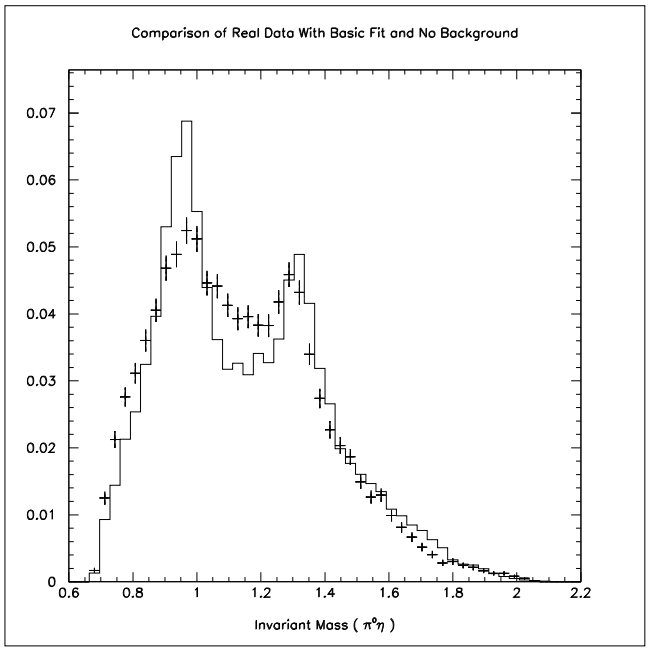

Figure 4.1: Comparison of $(\eta\pi^0)$ mass distribution for the real data and fit. The real data are represented by error bars. The fit contains channels 1$\rightarrow$4.

4.3 Inclusion of $\eta_2(1650)$

As stated in the introduction, the motivation for this analysis is to find states with $J^{PC}=2^{-+}$. A 2^{-+} meson can be formed by combining an $a_2(1320)$ $[J^{PC}=2^{++}]$ with a π^0 $[J^{PC}=0^{-+}]$, assuming zero orbital angular momentum between the $a_2(1320)$ and π^0. With zero electric charge, the 2^{-+} state has isospin, I=0. According to the

naming convention of the Particle Data Group, this state is called the η_2. Within this section, evidence for the first observation of the η_2 is presented.

The comparison of the $(\pi^0\pi^0\eta)$ mass distribution for the real and acceptance corrected phase space Monte Carlo data (Figure 3.2) shows a large enhancement in the (1500-1900)MeV mass region. This mass region was investigated by selecting several mass bands of $(\pi^0\pi^0\eta)$. In the case that the $\pi_i^0\pi_j^0\eta$ combination occurred in a selected mass band, then $(\pi_i^0\pi_j^0)$ was plotted versus $(\pi_i^0\eta)$ and $(\pi_j^0\eta)$. These scatter plots can be found in Figure 4.2. There is an important distinction between these scatter plots and Figure 3.4. On the latter figure, the pion used in the $\eta\pi$ combination is distinct from the two pions used in the combination plotted vertically. In all, six combinations contribute to this figure. On Figure 4.2, the objective is to study $X \to \eta\pi_i^0\pi_j^0$; the third pion, π_k^0, is the spectator. Along the horizontal axis the η is combined with both π_i^0 and π_j^0 forming X (2 combinations).

Figure 4.2 reveals an enhanced $a_2(1320)$ signal in the (1550-1750)MeV $\pi^0\pi^0\eta$ mass region relative to the (1350-1550)MeV and (1750-1950)MeV $\pi^0\pi^0\eta$ mass regions. This suggests a resonance in the (1550-1750)MeV mass region that decays into $a_2(1320)\pi^0$. Based on this evidence, the channel involving the η_2 decaying into $a_2(1320)\pi^0$ was included:

$$\bar{p}p \to \pi^0\eta_2 \to \pi^0[\pi^0 a_2(1320)] \to \pi^0\pi^0(\pi^0\eta) \qquad \text{Channel 5}$$

The mass and width of the η_2 were found to be M(η_2)=1650MeV and $\Gamma(\eta_2)$=180MeV. The addition of the η_2 hypothesis without interferences improved the fit by Δs=-13. Allowing interference between $\bar{p}p \to \pi^0\eta_2$ and $\bar{p}p \to \sigma.a_2(1320)$ improved the log likelihood further by Δs=-63. The mass of the η_2 was varied to ascertain the optimum mass. Figure 4.3 shows the variation of log likelihood with η_2 mass, with and without the phase space term. The removal of the background term increases the log likelihood by Δs=+221. The log likelihood profile without the background term has had 221 subtracted from the log likelihood values so that the two profiles have the same value when the fitted η_2 mass was 1650MeV.

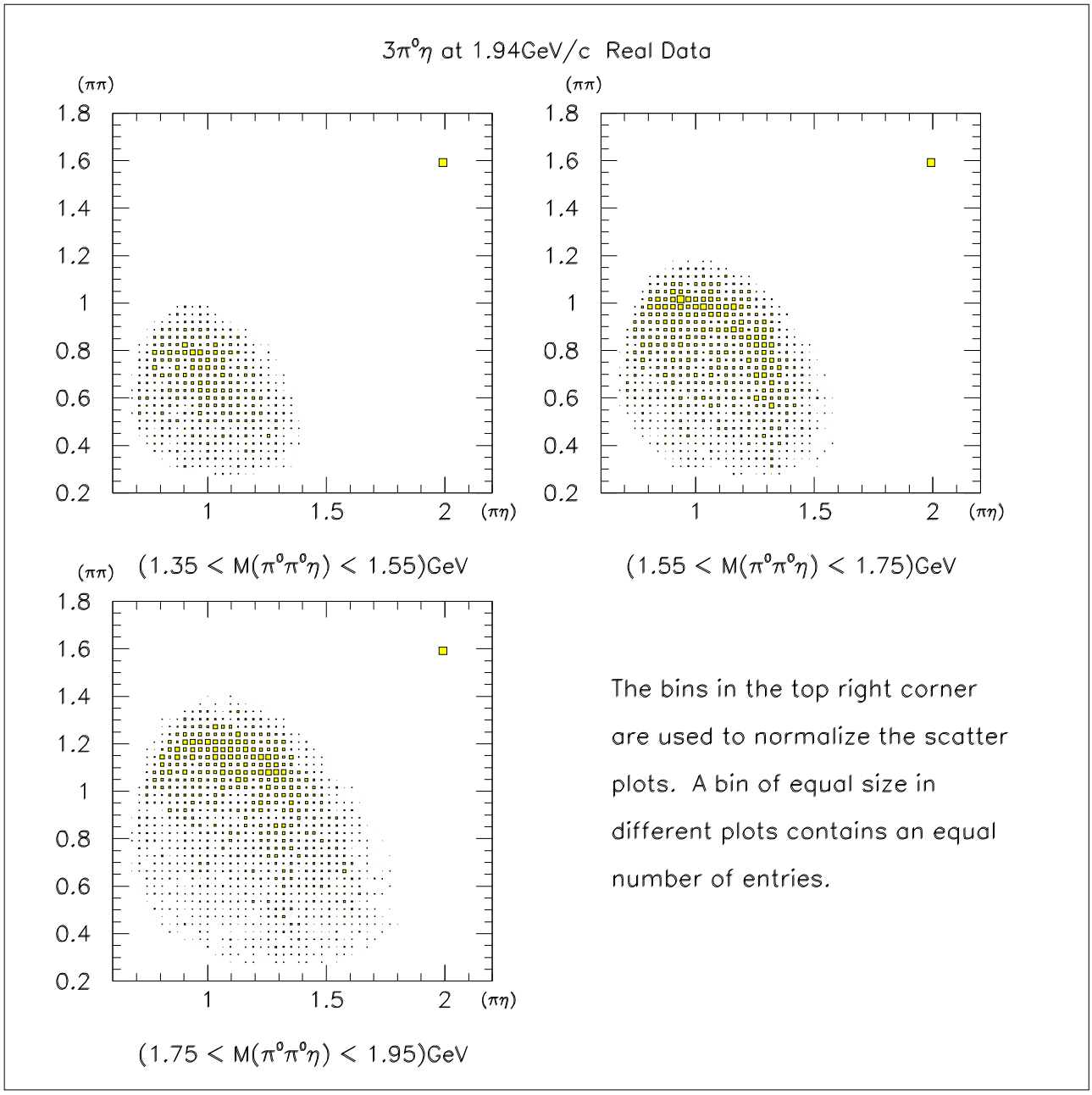

Figure 4.2: For a mass band of $\pi_i^0\pi_j^0\eta$, ($\pi_i^0\pi_j^0$ vs $\pi_i^0\eta$) and ($\pi_i^0\pi_j^0$ vs $\pi_j^0\eta$) has been plotted. The (1.55-1.75)GeV mass band shows an enhanced $a_2(1320)$ signal relative to the lower and upper $\pi^0\pi^0\eta$ mass bands.

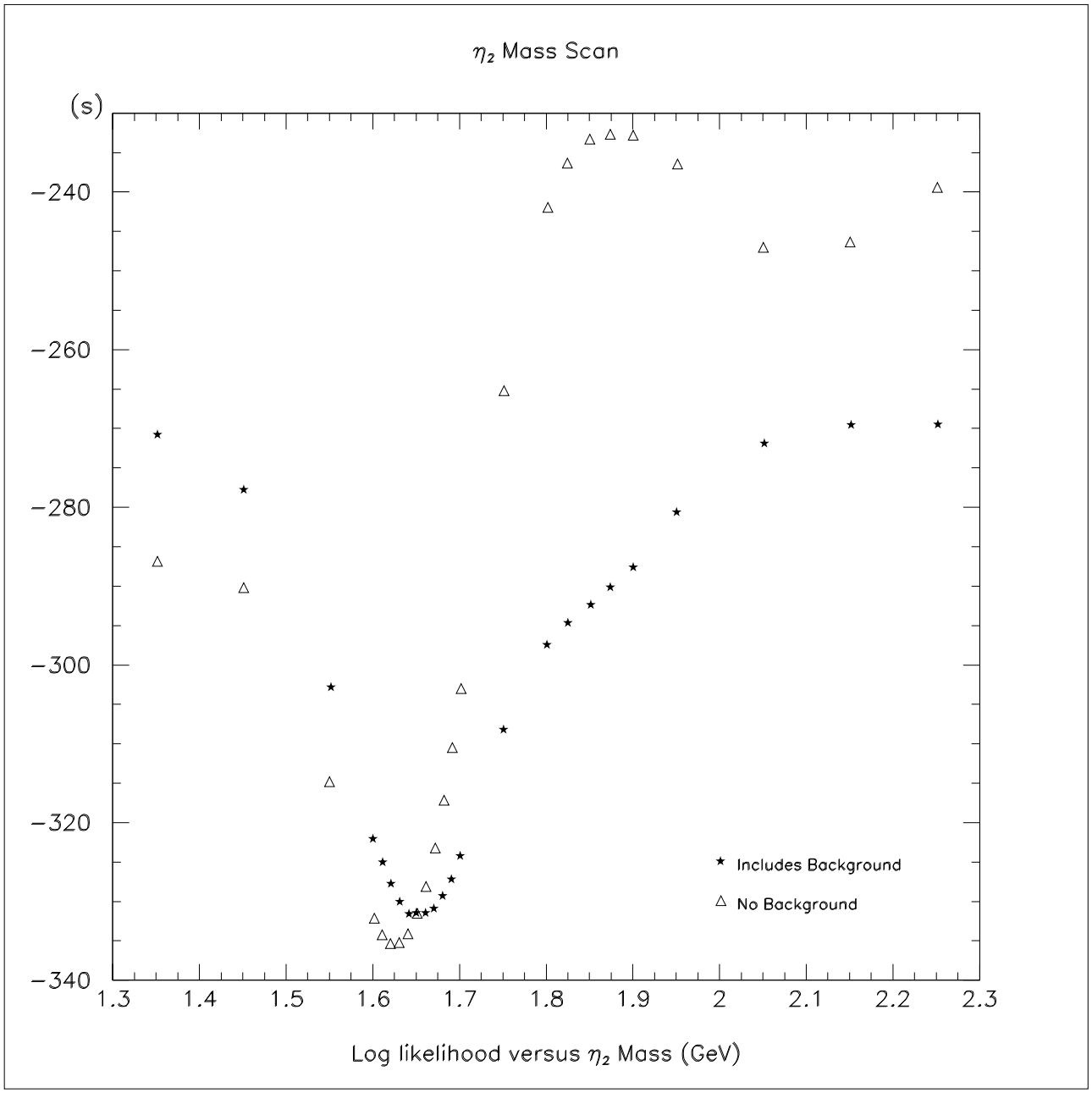

Figure 4.3: Mass scan for the η_2. An η_2 width of 180MeV is assumed. The profile with triangular data points represents the mass scan without the phase space term and has had the log likelihood values adjusted to agree with the plot including background at 1650MeV.

Both the log likelihood profiles show a large dip at about 1650MeV. The depth and gradient of the dips strongly suggest that a resonance is required in this mass region. Using the fit that includes the background term, the resonance mass is 1650MeV. This profile was chosen since (a) it gives a better log likelihood, (b) the sides of the dip are more evenly balanced and (c) the dip appears in both profiles and therefore is not a feature produced by the background term.

The mass scan profile without the background term shows a wide dip around 2135MeV. The mass scan profile including the background term appears to have a linear region between 1800 and 1900MeV. Both these features are discussed in later sections and correspond to further resonances.

The width of the η_2 was varied assuming a mass of 1650MeV. The η_2 width shows (Figure 4.4) little variation with log likelihood, but a value of 180MeV gives the best fit. The background term increases the width of the dip, but has only a small effect on the optimum.

The sharp mass definition is explained by the interference between the $\pi^0\eta_2(1650)$ and $a_2(1320)\sigma$ channels. The width is less well defined because other ingredients in the fit are capable of taking up the slack when the width is altered.

To test the hypothesis of the resonance being $J^{PC}=2^{-+}$, alternative spin states were substituted and the assumed mass of the resonance was varied. The log likelihood values corresponding to resonance mass and spin, (assuming a width of 180MeV), can be found in Table 4.1.

The results in Table 4.1 provide strong evidence that the resonance has $J^{PC}=2^{-+}$ with a mass of 1650MeV. Additional (and alternative) channel combinations were included with (or replaced) the $\pi^0\eta_2(1650)$ channel. Such channels (eg $X \to a_0(980)\pi^0$ and $X \to a_2(1320)\pi^0$) with orbital angular momentum L=0,1,or 2 gave no significant signal.

Assuming that the resonance is a normal $q\bar{q}$ state, then this constitutes the first observation of the η_2. A discussion of the errors in the measurement of the η_2 mass and width can be found in a later section.

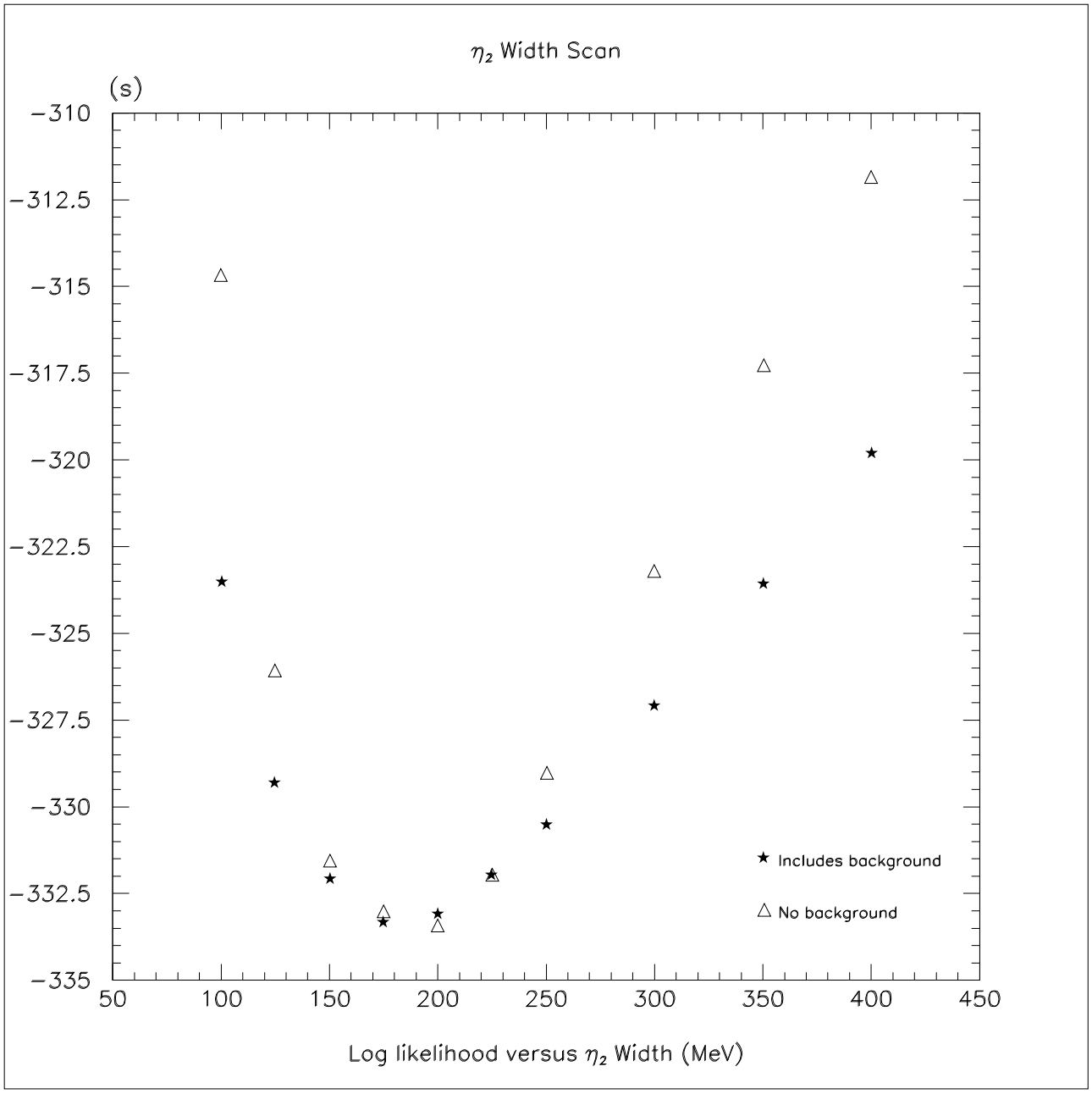

Figure 4.4: Width scan for the η_2. An η_2 mass of 1650MeV is assumed. The profile with triangular data points represents the mass scan without the background term and has had the log likelihood values adjusted for the benefit of comparison.

M($\pi^0\pi^0\eta$) (MeV)	2^{-+} $[a_2(1320)\pi^0]_{L=0}$	1^{++} $[a_2(1320)\pi^0]_{L=1}$	2^{++} $[a_2(1320)\pi^0]_{L=1}$	3^{++} $[a_2(1320)\pi^0]_{L=1}$
1350	-271	-258	-206	-263
1450	-278	-271	-205	-266
1550	-303	-279	-209	-268
1650	-332	-261	-213	-254
1750	-308	-227	-209	-221
1850	-292	-205	-206	-201

Table 4.1: The log likelihood values determined using various spin and mass assumptions. The L=1 centrifugal barrier used a radius of interaction of 0.6fm.

4.4 Inclusion of $\pi_2(1670)$

The comparison of the $(\pi^0\pi^0\pi^0)$ mass distribution for the real and acceptance corrected phase space Monte Carlo data (Figure 3.2) shows a large discrepancy around 1700MeV. A candidate for the source of this enhancement in the real data is the isospin I=1 partner of the $\eta_2(1650)$. Assuming the strongest decay mode of the $\pi_2(1670)$ into $f_2(1270)\pi$, the $\eta\pi_2(1670)$ channel was included in the fit:

$$\bar{p}p \to \eta\pi_2(1670) \to \eta[\pi^0 f_2(1270)] \to \eta\pi^0(\pi^0\pi^0) \qquad \text{Channel 6}$$

The addition of the $\eta\pi_2(1670)$ channel improves the fit by Δs=-142. Including interference with other channels, $a_0(980)f_2(1270)$ and $\pi^0\eta_2(1650)$ further improves the fit by Δs=-25.3 and Δs=-10.4 respectively. For further evidence of the $\pi_2(1670)$, a cut on events with $f_2(1270)$ was made. If a $(\pi^0\pi^0)$ mass was measured to be between (1100-1400)MeV and the $(\pi^0\eta)$ mass was not in the $a_2(1320)$ [(1318.2$\pm$75)MeV] mass region, the $(\pi^0\pi^0\pi^0)$ was plotted: see bottom of Figure 4.13. No $\pi_2(1670)$ peak is evident in this $(\pi^0\pi^0\pi^0)$ mass distribution. However, due to the significant

improvement to the log likelihood and the $(\pi^0\pi^0\pi^0)$ enhancement in the complete mass distribution plot, the $\pi_2(1670)$ was retained in the fit.

4.5 Inclusion of X(2135)

The log likelihood profile in the $\eta_2(1650)$ mass scan (without the background term), Figure 4.3, reveals a dip as the fitted η_2 (ie $\pi^0\pi^0\eta$) mass is scanned at a high mass. To identify the source of this dip, scatter plots (of the same format as those found in Figure 4.2) were constructed for three mass regions of $\pi^0\pi^0\eta$ and can be found in Figure 4.5.

In the $\pi^0\pi^0\eta$ (1950-2150)MeV mass region, a large $a_2(1320)$ and $f_2(1270)$ enhancement occurs where the two signals cross. This suggests interference between

$$X \to a_2(1320)\pi^0 \qquad \text{Channel 7}$$

and

$$X \to f_2(1270)\eta \qquad \text{Channel 8}$$

It is not due to $a_2(1320)f_2(1270)$. The threshold for this process is at 2590MeV, far above the available centre of mass energy 2409MeV. Trials were made adding this channel to the analysis, but it gave negligible improvement. If this process were important, it should show up on the right-hand edge of Figure 3.4, near the intersection of $a_2(1320)$ and $f_2(1270)$ bands, but no strong signal is evident there.

The magnitude of the enhancement is also too large to be produced by interference between channels 1 and 2 and therefore one or more resonances in this high $\pi^0\pi^0\eta$ mass region are required. The quark model predicts several mesons in the 2000-2100MeV mass range: ${}^3F_4(4^{++})$, ${}^3F_3(3^{++})$ and ${}^3F_2(2^{++})$. Also predicted is the ${}^1G_4(4^+)$ which is expected in the (2200-2350)MeV mass region. To determine the *dominant* contribution to the $a_2(1320).f_2(1270)$ interference cross, a single resonance was included into the fit and a large number of spin states tested. Fully coherent

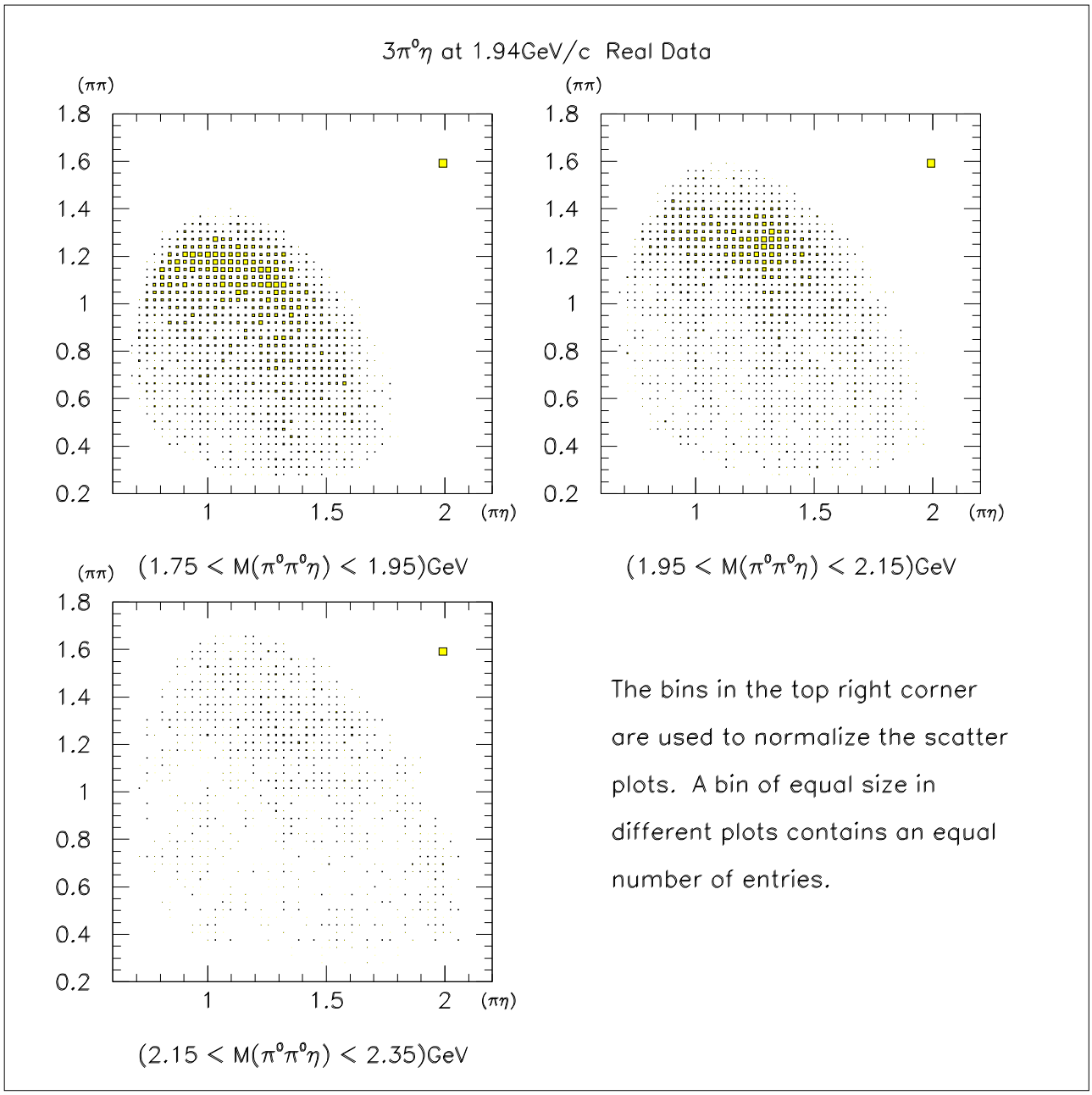

Figure 4.5: For a mass band of $\pi_i^0\pi_j^0\eta$, ($\pi_i^0\pi_j^0$ vs $\pi_i^0\eta$) and ($\pi_i^0\pi_j^0$ vs $\pi_j^0\eta$) has been plotted.

interference between channel 6 and 7 was assumed. For $X \rightarrow a_2(1320)\pi^0$ and $X \rightarrow f_2(1270)\eta$ with orbital angular momentum, L=0,1 or 2, there are the following possibilities:-

- 2^{-+} [L=0]
- 3^{++}, 2^{++}, 1^{++} [L=1]
- 4^{-+}, 3^{-+}, 2^{-+}, 1^{-+}, 0^{-+} [L=2]

These and several more spin states were tested and the resulting improvements to the log likelihood can be found below.

- **L = 3**
  - 4^{++} Δs = -0.2
- **L = 2**
  - 4^{-+} Δs = -3.4
  - 3^{-+} Δs = -8.0
  - 2^{-+} Δs = -1.1
  - 1^{-+} Δs = -1.6
  - 0^{-+} Δs = -10.3
- **L = 1**
  - 3^{++} Δs = -10.0
  - 2^{++} Δs = -46.0 $\rightarrow$ Only significant contribution.
  - 1^{++} Δs = -6.1
- **L = 0**
  - 2^{-+} Δs = -13.0

The only significant signal (Δs=-46) comes from 2^{++}. This is surprising since a 2^{++} resonance is expected to decay preferentially into $\pi\pi$ and 4π. The optimised mass and width for the 2^{++} state are 2135MeV and 250MeV respectively. It can be construed that this is the same resonance seen by GAMS[42] in $X \to \eta\eta$ with a mass of (2175±20)MeV and width (150±35)MeV. Substituting the GAMS resonance for the optimum fit, the log likelihood deteriorates by just Δs=+5.

It is found that the $\eta\pi_2(1670)$ channel has similar kinematics to the $\pi^0 X(2135)$ channel and is therefore able to compensate within the fit when the $\pi^0 X(2135)$ channel is removed. Without the inclusion of the $\eta\pi_2(1670)$ channel, the removal of the $\pi^0 X(2135)$ channel makes the fit deteriorate by Δs=+105. Therefore the already significant contribution of the $\pi^0 X(2135)$ channel with Δs=-46 should be considered as a lower limit.

The effect of the $\pi^0 X(2135)$ channel upon the $\pi^0\eta_2(1650)$ channel is found to be negligible. The mass and width scan for the $X(2135)$ can be seen in Figure 4.6. The mass scan assumed an $X(2135)$ width of 250MeV and the corresponding width scan assumed a mass of 2135MeV. Similar to the $\eta_2(1650)$ width scan, the log likelihood is fairly insensitive to the assumed width of the $X(2135)$. Note that the mass and width scans were carried out with the optimum fit (including the $\pi_2(1670)$) which is described in the summary.

4.6 Inclusion of X(1850)

The scatter plot from the (1.75-1.95)GeV $\pi^0\pi^0\eta$ mass region in Figure 4.5 has a strong $f_2(1270)$ band, corresponding to $X \to f_2(1270)\eta$. The mass of the $f_2(1270)$ appears to be low, in this plot and in Figure 3.4, suggesting that the $f_2(1270)$ is strongly produced at threshold. With this in mind (and the strangely linear region of the log likelihood profile from the $\eta_2(1650)$ scan), events with a $(\pi^0\pi^0)$ mass in the region (1075-1425)MeV *ie* the $f_2(1270)$ region, were selected and the corresponding $(\pi^0\pi^0\eta)$ mass plotted. Figure 4.7 compares the above $(\pi^0\pi^0\eta)$ mass distribution with

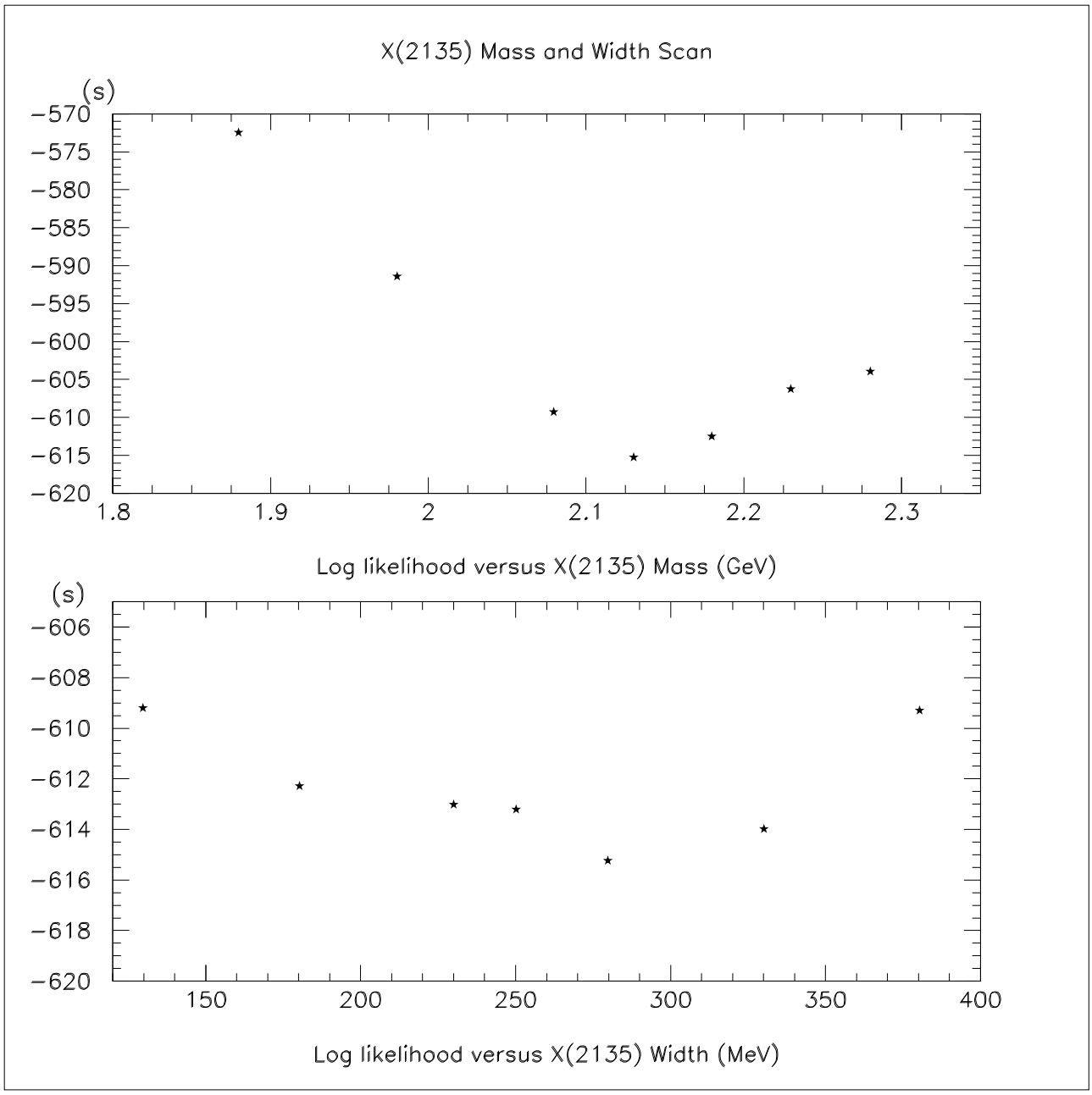

Figure 4.6: Mass and width scan for $X(2135)$.

that of acceptance corrected phase space Monte Carlo data. Note that the two mass distributions have been arbitrarily normalized such that the area under the profile is unity. A clear enhancement is seen from 1760 to 1900MeV in the real data.
A resonance was added to the fit with an 1850MeV mass and 225MeV width in the channel:

$$\bar{p}p \rightarrow \pi^0 X(1850) \rightarrow \pi^0[\eta f_2(1270)] \rightarrow \pi^0\eta(\pi^0\pi^0) \qquad \text{Channel 9}$$

A resonance close to the $\eta f_2(1270)$ threshold is very likely to have orbital angular momentum L=0, hence quantum numbers $J^{PC}=2^{-+}$. However, as with the tests for the $\pi^0 X(2135)$ channel, many spin states were tested for the $X(1850)$ state. The optimum fit was given by 2^{-+} with Δs=-54. This fit included $X(1850)$ interfering with the $a_0(980)f_2(1270)$, $\eta\pi_2(1670)$ and $\pi^0\eta_2(1650)$ channels. Table 4.2 presents the results of alternative mass and spin assignments to the resonance with an $\eta f_2(1270)$ decay mode.
A potential explanation of the strong $f_2(1270)$ band without requiring an additional resonance is that the $\eta f_2(1270)$ signal is due a second decay mode of the $\eta_2(1650)$ in it's high energy tail. This solution has been rejected. A Flatté formula was used to fit the $\eta_2(1650)$, enabling it to decay into $a_2(1320)\pi^0$ and $\eta f_2(1270)$.

$$f_i = \frac{\Lambda_i (M\Gamma_i)_r}{s - M^2 + iM(\Gamma_1 + \Gamma_2)} \tag{4.6}$$

Here $(M\Gamma_i)_r$ implies evaluation on resonance with mass, M=1650MeV. The term $\Gamma(a_2(1320)\pi^0)$ is kept constant, but allowance is made for the opening of the $f_2(1270)\eta$ channel by using a Fermi function:

$$\Gamma_2 = \frac{\Gamma_1 \sum_m \mid \Lambda_{2m} \mid^2 / (7 \sum_m \mid \Lambda_m \mid^2)}{1 + exp([3.323 - s]/0.3458)} \tag{4.7}$$

The numerator weights Γ_2 by the sum of intensities of helicities m=0, 1 and 2 for the second channel and divides by the corresponding sum for the first channel. The factor 7 is used to allow for the 14% branching ratio of $a_2(1320)$ into $\eta\pi$. The

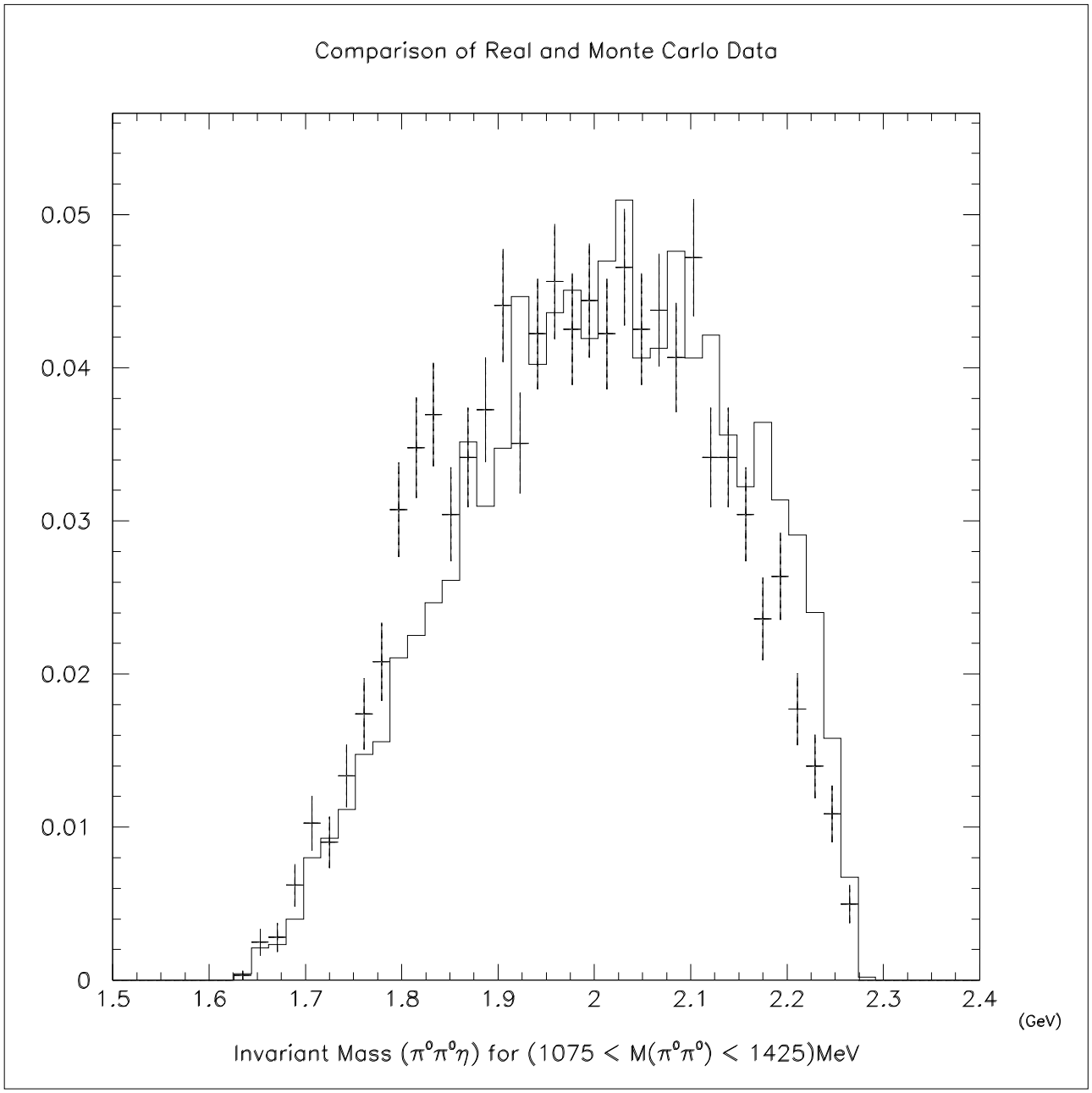

Figure 4.7: Comparison of real and Monte Carlo data for the $(\pi^0\pi^0\eta)$ mass in which the $(\pi^0\pi^0)$ mass is in the $f_2(1270)$ mass region. Error bars represent the real data.

M($\pi^0\pi^0\eta$) (MeV)	3^{++} $[\eta f_2(1270)\pi^0]_{L=1}$	2^{++} $[\eta f_2(1270)\pi^0]_{L=1}$	1^{++} $[\eta f_2(1270)\pi^0]_{L=1}$
1600	47.2	16.2	5.3
1650	39.2	21.0	8.3
1700	31.8	23.8	9.8
1750	28.5	22.4	10.2
1800	26.0	21.5	11.5
1850	23.8	20.8	12.2
1900	22.2	17.9	11.5
1950	20.2	15.1	10.9
2000	21.1	15.1	10.8

Table 4.2: Improvements to log likelihood using various spin and mass assumptions for the $X(1850)$. The L=1 centrifugal barrier used a radius of interaction of 0.6fm.

denominator is an approximation to the opening of the $\eta f_2(1270)$ channel. The width of the $f_2(1270)$ is included in the factor 0.3458; however, the fit results are insensitive to this number.

The resulting fit gives a poor description of the energy dependence of $\eta f_2(1270)$ production: Δs=-12 compared with -54 when the 1850MeV resonance is fitted independently. Fitting the data with two separate resonances gives a far superior log likelihood compared with that from a single resonance with a Flatté formula. Both the $\eta_2(1650)$ and $X(1850)$ interfere strongly with other channels. The pattern of interference is quite different for the two resonances suggesting that they are independent signals.

The assignment of this state to the 2^{-+} nonet is difficult. A possibility is the η_2'; a predicted state analogous to the $\eta'(958)$ of the pseudoscalar nonet. However, it is expected that the η_2' should have a dominant decay mode into $K\bar{K}\pi$. The decay to $\eta f_2(1270)$ is tentative evidence for a glueball since gluons are believed to couple preferentially to η and η'. It is interesting that MARK III data on $J/\psi \to \gamma(\eta\pi\pi)$ shows a clear peak at 1850MeV in $\eta\pi\pi$, Figure 4.8(a). No spin-parity analysis of these data has been published.

There is some other evidence for $X(1850)$. The Crystal Ball $\gamma\gamma \to \pi^0\pi^0\eta$ data[43] shows a signal near 1900MeV, Figure 4.8(b). They claimed a 2^{-+} state with a large (70%) decay into $a_2(1320)\pi^0$ and 30% decay into $a_0(980)\pi$. Adding an $a_2(1320)\pi^0$ decay mode for the 2^{-+} $X(1850)$ to the optimum fit gave no significant improvement. Data from the VES Spectrometer at Serpukhov have shown a signal[44] at 1815MeV in $\pi^-\eta\eta$ with spins 1^{++} and 2^{-+} favoured. This cannot be the same state as the $X(1850)$ found here, due to isospin.

4.7 Mass and Width Errors

The systematic errors in the measured masses and widths of the resonances were estimated from the range of fitted values as the ingredients in the fit were varied.

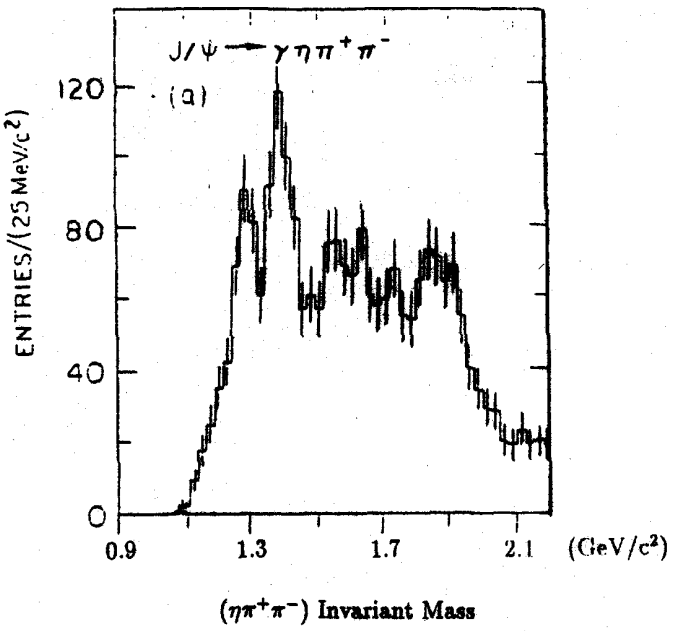

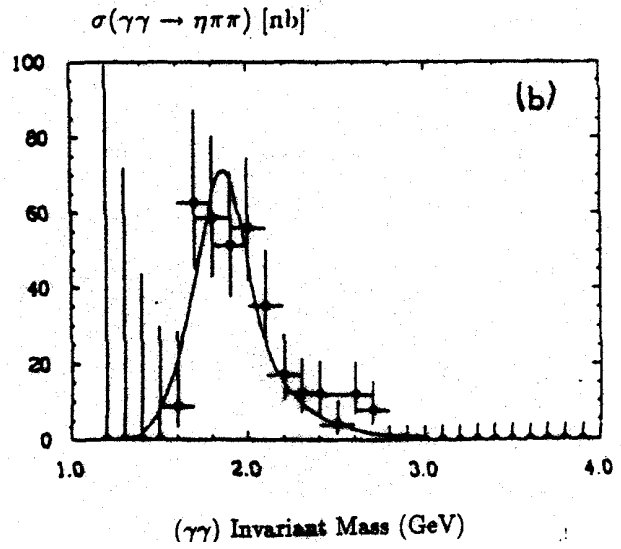

Figure 4.8: (a) MARK III $J/\psi \to \gamma\eta\pi^+\pi^-$ data. The $(\eta\pi^+\pi^-)$ invariant mass distribution shows a peak at 1850MeV. (b) Crystal Ball $\gamma\gamma \to \eta\pi^0\pi^0$ data. The cross section peaks in the $(\gamma\gamma)$ invariant mass region just below 1900MeV.

The statistical errors are considered to be negligible compared to the systematic errors. The estimated errors cover the full range of variation observed with different ingredients in the fit. Table 4.3 summarizes the errors on resonance mass and width.

Resonance	Mass (M)	Δ M	Width (Γ)	Δ Γ
$\eta_2(1650)$	1650	$\pm$ 15	180	$\pm$ 75
$X(1850)$	1850	$\pm$ 30	225	$\pm$ 50
$X(2135)$	2135	$\pm$ 50	250	$\pm$ 50

Table 4.3: Resonance Mass and Widths including the estimated errors.

4.8 Summary

The optimum fit to the $\bar{p}p \to \pi^0\pi^0\pi^0\eta$ at 1.94GeV/c required the following channels:-

$\bar{p}p \to \mathrm{f}_2(1270).a_0(980) \to (\pi^0\pi^0)(\pi^0\eta)$ Channel 1

$\bar{p}p \to \sigma.a_2(1320) \to (\pi^0\pi^0)(\pi^0\eta)$ Channel 2

$\bar{p}p \to \pi^0 f_1(1285) \to \pi^0[\pi^0 a_0(980)] \to \pi^0\pi^0(\pi^0\eta)$ Channel 3

$\bar{p}p \to \sigma.a_0(980) \to (\pi^0\pi^0)(\pi^0\eta)$ Channel 4

$\bar{p}p \to \pi^0\eta_2 \to \pi^0[\pi^0 a_2(1320)] \to \pi^0\pi^0(\pi^0\eta)$ Channel 5

$\bar{p}p \to \eta\pi_2(1670) \to \eta[\pi^0 f_2(1270)] \to \eta\pi^0(\pi^0\pi^0)$ Channel 6

$\bar{p}p \to \pi^0 X(2135) \to \pi^0[\pi^0 a_2(1320)]$ and $\pi^0[\eta f_2(1270)]$ Channel 7 & 8

$\bar{p}p \to \pi^0 X(1850) \to \pi^0[\eta f_2(1270)] \to \pi^0\eta(\pi^0\pi^0)$ Channel 9

An indication of the significance of the contribution from a channel is given by the change in log likelihood when the channel is removed from the optimum fit. This change can be considered as a lower limit since channels with similar kinematics are able to compensate to some extent when the fit is re-optimized. An example of this effect can be seen with the $\eta\pi_2(1670)$ and $\pi^0 X(2135)$ channels. Table 4.4 presents the effect of dropping individual channels. Without the $\eta\pi_2(1670)$ channel, the $\pi^0 X(2135)$ makes a highly significant contribution to the fit since the $\eta\pi_2(1670)$ is not there to compensate. The $\eta\pi_2(1670)$ channel is not easily seen by eye in the data (See bottom of Figure 4.13) and causes ambiguity in the fit, but it is retained since it is an established resonance and provides a significant improvement to the log likelihood. Without the $\eta\pi_2(1670)$ channel, the $\pi^0\eta_2(1650)$ and $a_0(980)f_2(1270)$ channels become slightly less significant. This can be attributed to the removal of the interference with the $\eta\pi_2(1670)$.

Drop Channel	With $\eta\pi_2(1670)$	Without $\eta\pi_2(1670)$
$\eta\pi_2(1670)$	$\Delta s = +88.0$	
$\pi^0\eta_2(1650)$	$\Delta s = +67.6$	$\Delta s = +50.2$
$\pi^0 X(1850)$	$\Delta s = +53.8$	$\Delta s = +103.4$
$\pi^0 X(2135)$	$\Delta s = +37.6$	$\Delta s = +101.2$
$a_0(980)f_2(1270)$	$\Delta s = +29.2$	$\Delta s = +20.7$
$a_2(1320)\sigma$	$\Delta s = +16.3$	$\Delta s = +18.7$
$a_0(980)\sigma$	$\Delta s = +12.8$	$\Delta s = +18.2$
$\pi^0 f_1(1285)$	$\Delta s = +41.5$	$\Delta s = +42.4$
Background	$\Delta s = +69.2$	$\Delta s = +91.3$

Table 4.4: The effect of dropping individual components from the optimum fit, with and without the inclusion of the $\eta\pi_2(1670)$ channel.

Interference plays an important part in the data with the prominent channels 1 and 2 acting as interferometers. Phase information from the interference makes the fit sensitive to the resonance masses thus helping to establish the masses of resonances with broad widths. Interferences improving the log likelihood by more than Δs=-10 were retained in the fit:-

$$a_0(980)f_2(1270) \otimes \pi^0 X(1850) : \Delta s = \text{-}21.2$$

$$a_2(1320)\sigma \otimes \pi^0\eta_2(1650) : \Delta s = \text{-}30.1$$

$$\pi^0\eta_2(1650) \otimes \pi^0 X(1850) : \Delta s = \text{-}20.1$$

$$a_0(980)f_2(1270) \otimes \eta\pi_2(1670) : \Delta s = \text{-}25.3$$

$$\pi^0\eta_2(1650) \otimes \eta\pi_2(1670) : \Delta s = \text{-}10.4$$

$$\pi^0 X(1850) \otimes \eta\pi_2(1670) : \Delta s = \text{-}34.2$$

The comparison of the real data with the invariant mass projections from the optimum fit provides a good illustration of the overall quality of the fit. These mass projections can be found in Figures 4.9 and 4.10. Figure 4.11 shows the full scatter plot generated by the optimum fit. Resonances with narrow widths in the fit projections are slightly too broad. This may be because the phase space component is not a perfect description of the background.

More specific regions of the data, such as the data with $\pi^0\eta$ combinations in the $a_2(1320)$ mass region have been selected to illustrate a more detailed comparison of the real data with the optimum fit. Figure 4.12 shows the $(\pi^0\pi^0\eta)$ mass distribution for events with a $(\pi^0\eta)$ mass combination in the $a_2(1320)$ mass region ([1318.2$\pm$75]MeV) and a cut against the $f_0(975)$ and $f_2(1270)$. Enhancements around 1650MeV and 2135MeV show clear $\eta_2(1650)$ and $X(2135)$ signals. The latter is small since it's second decay mode via $\pi^0 f_2(1270)$ has been removed.

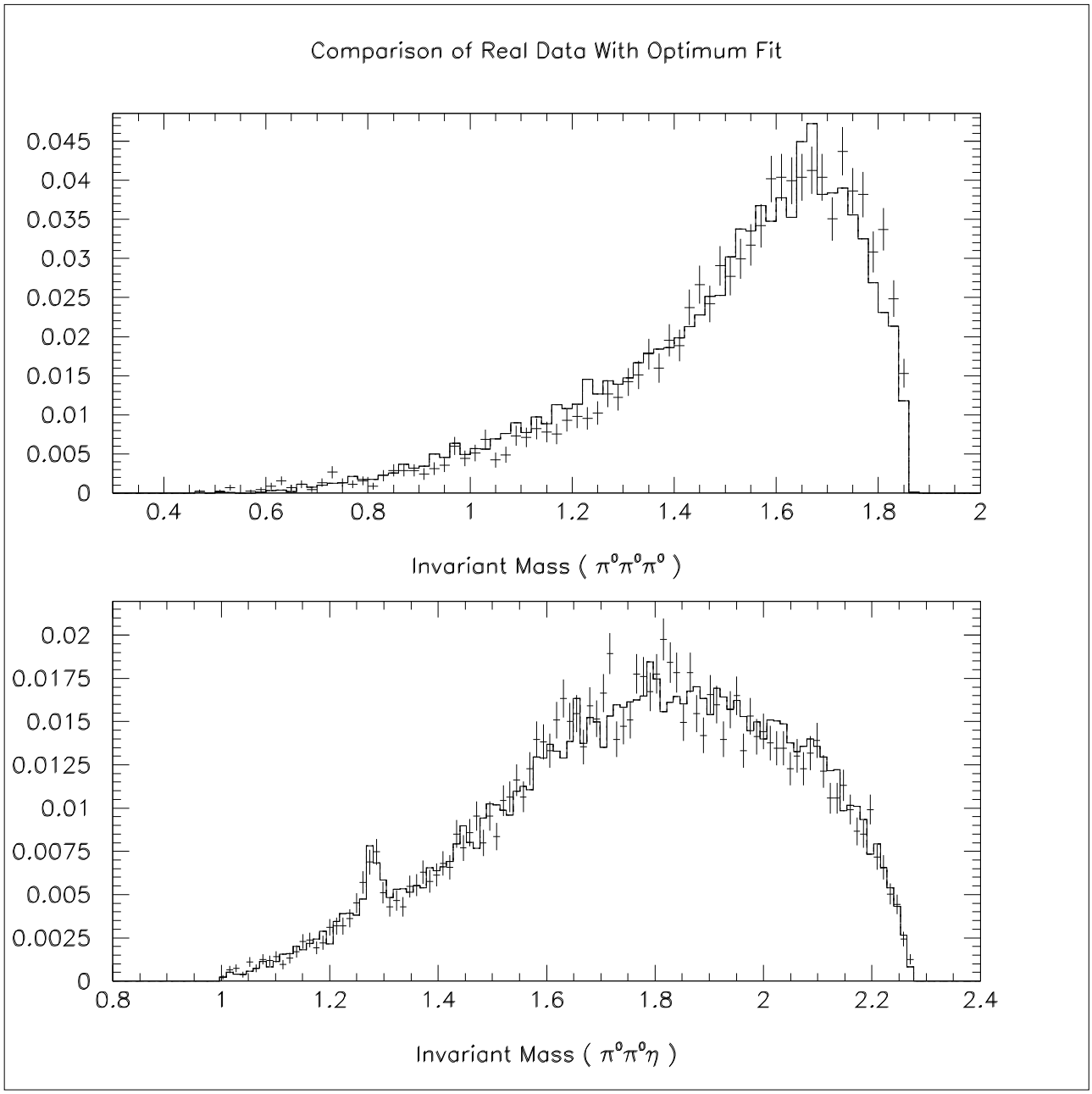

Figure 4.9: Comparison of real data with the optimum fit projections for $(\pi^0\pi^0\pi^0)$ and $(\pi^0\pi^0\eta)$. The real data is represented by the error bars.

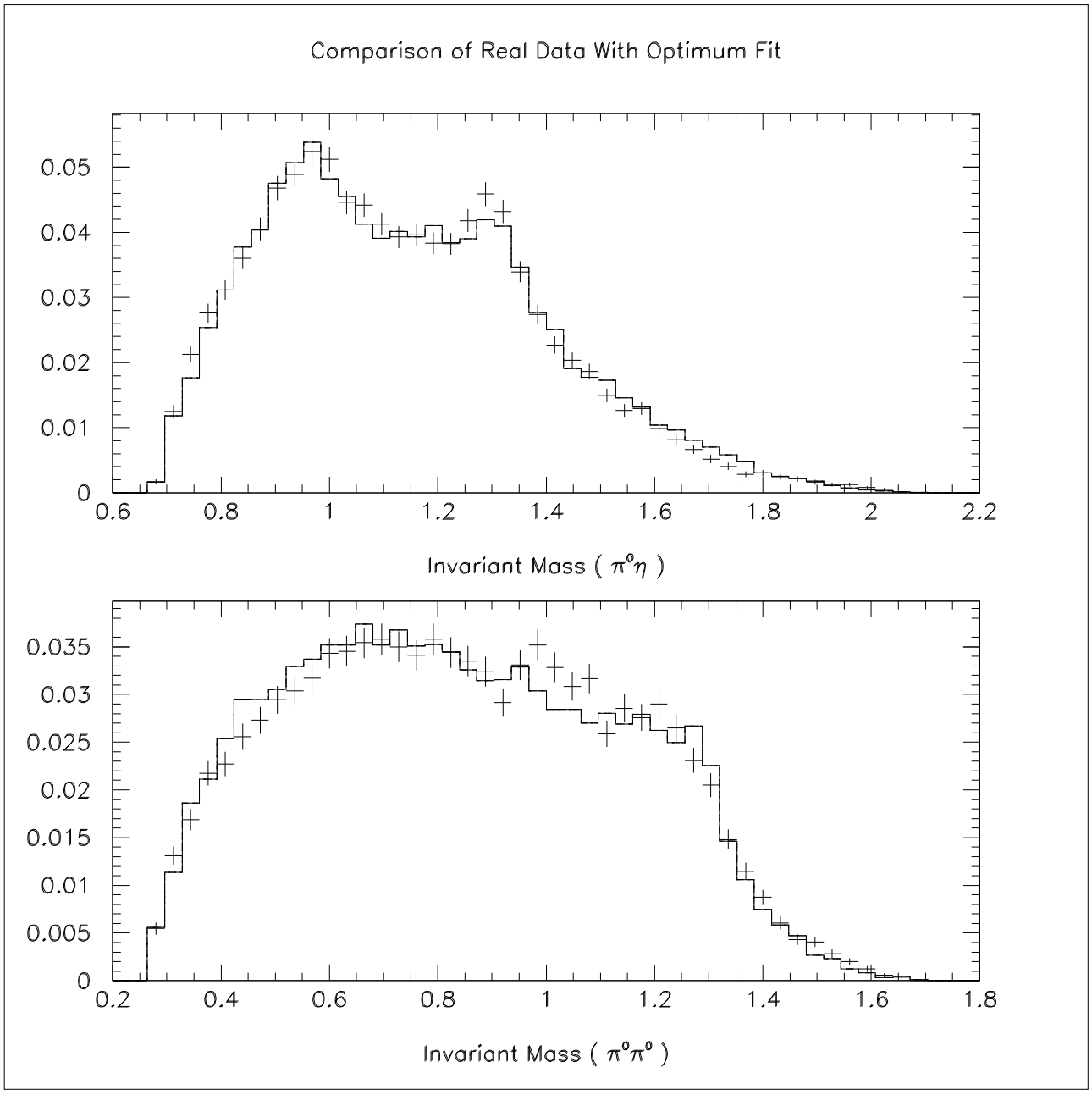

Figure 4.10: Comparison of real data with the optimum fit projections for $(\pi^0\eta)$ and $(\pi^0\pi^0)$. The real data is represented by the error bars. A small discrepancy can be seen in the $f_0(975)$ mass region.

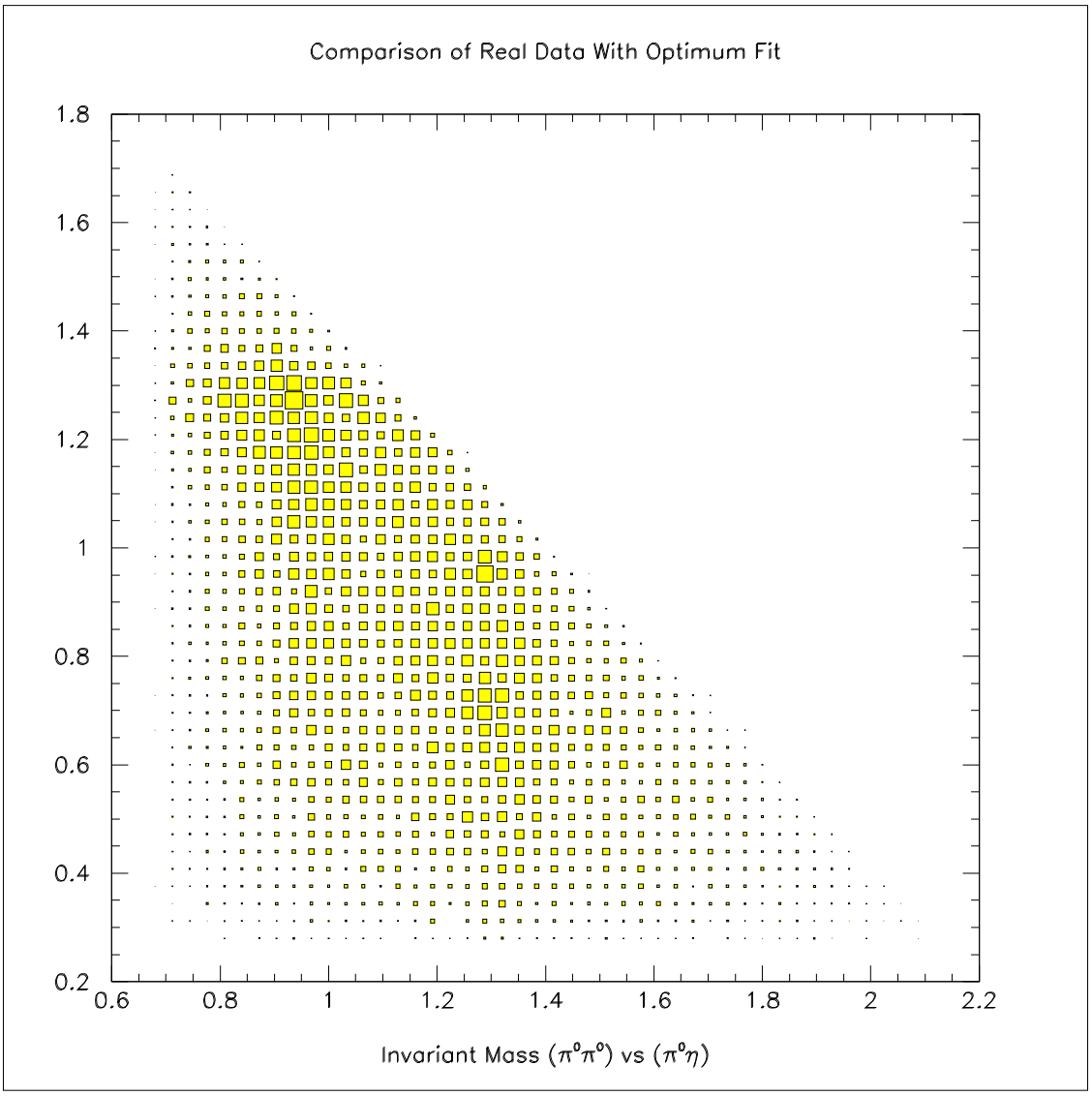

Figure 4.11: Full scatter plot of $(\pi^0\pi^0)$ versus $(\pi^0\eta)$ [all combinations plotted] generated using the optimum fit parameters. This compares well with the real data scatter plot in Figure 3.4

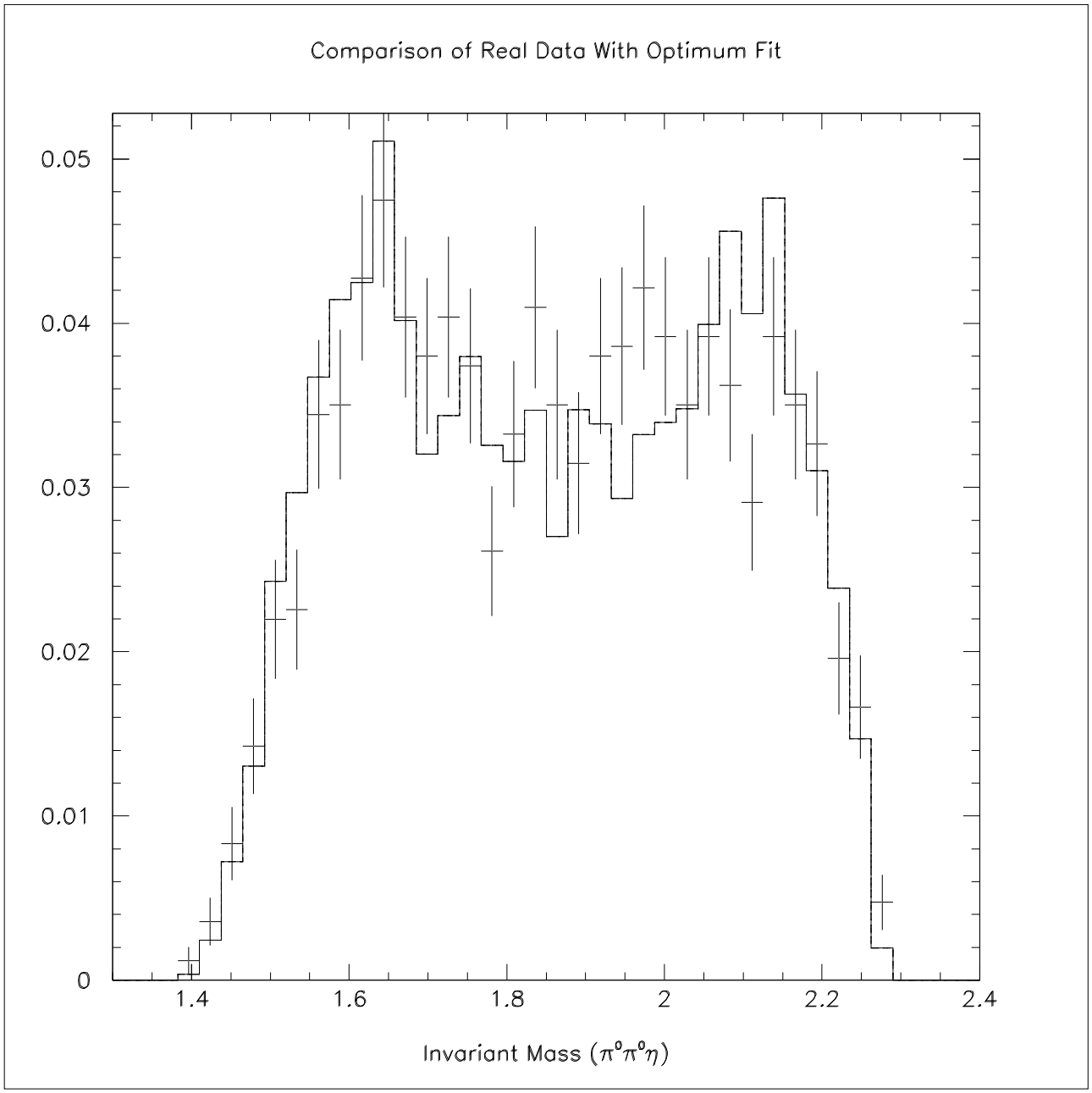

Figure 4.12: Comparison of real data with the optimum fit projections. This plot shows the $(\pi^0\pi^0\eta)$ mass with a $(\pi^0\eta)$ combination in the $a_2(1320)$ mass region and the $(\pi^0\pi^0)$ mass not in the region (925-1325)MeV to avoid the $f_0(975)$ and $f_2(1270)$. Error bars represent the real data.

Selecting events with $(\pi^0\pi^0)$ combinations in the $f_2(1270)$ mass region (1100-1400MeV) and cutting out those events which have a $(\pi^0\eta)$ combination in the $a_2(1320)$ mass region shows peaks due to the $X(1850)$ and $X(2135)$ in the resulting $(\pi^0\pi^0\eta)$ mass distribution, Figure 4.13. Also shown is the $(\pi^0\pi^0\pi^0)$ mass distribution. It is puzzling that there is no apparent signal from $\pi_2(1670) \to \pi^0 f_2(1270)$.

To check that a channel including the $a_0(980)$ had not been missed, events with a $(\pi^0\eta)$ combination in the mass region of the $a_0(980)$ ([982.7±70]MeV) were selected and the corresponding $(\pi^0\pi^0\eta)$ mass distribution plotted. Note that $(\pi^0\pi^0)$ combinations in the $f_2(1270)$ mass region were not used so as to eliminate the strong $a_0(980)f_2(1270)$ signal, channel 1. This $a_0(980)\pi^0$ mass distribution can be seen in Figure 4.14. There is no evidence for further resonances, in particular for the decays of $\eta_2(1650)$ or $X(1850)$ to $a_0(980)\pi^0$. Also presented is a $(\pi^0\pi^0\eta)$ mass distribution from events with a $(\pi^0\pi^0)$ mass in the region of the $f_0(975)$ ([974.1±50]MeV). This shows a slight systematic enhancement in the real data from 1575 to 1700MeV. On investigation, it is found that this discrepancy can be removed by adding a 0^- state (decaying into $f_0(975)\eta$) with a mass between (1625-1650)MeV. The addition improves the log likelihood by a barely significant amount, Δs=-21, and is ambiguous with a spin of 1^{++} which gives Δs=-15. Higher statistics would be needed to resolve whether a further resonance is required, and if so, it's spin-parity assignment. It is certainly not an additional decay mode of $\eta_2(1650)$. The L=2 centrifugal barrier is strong and consequently this hypothesis gives only Δs=-4.

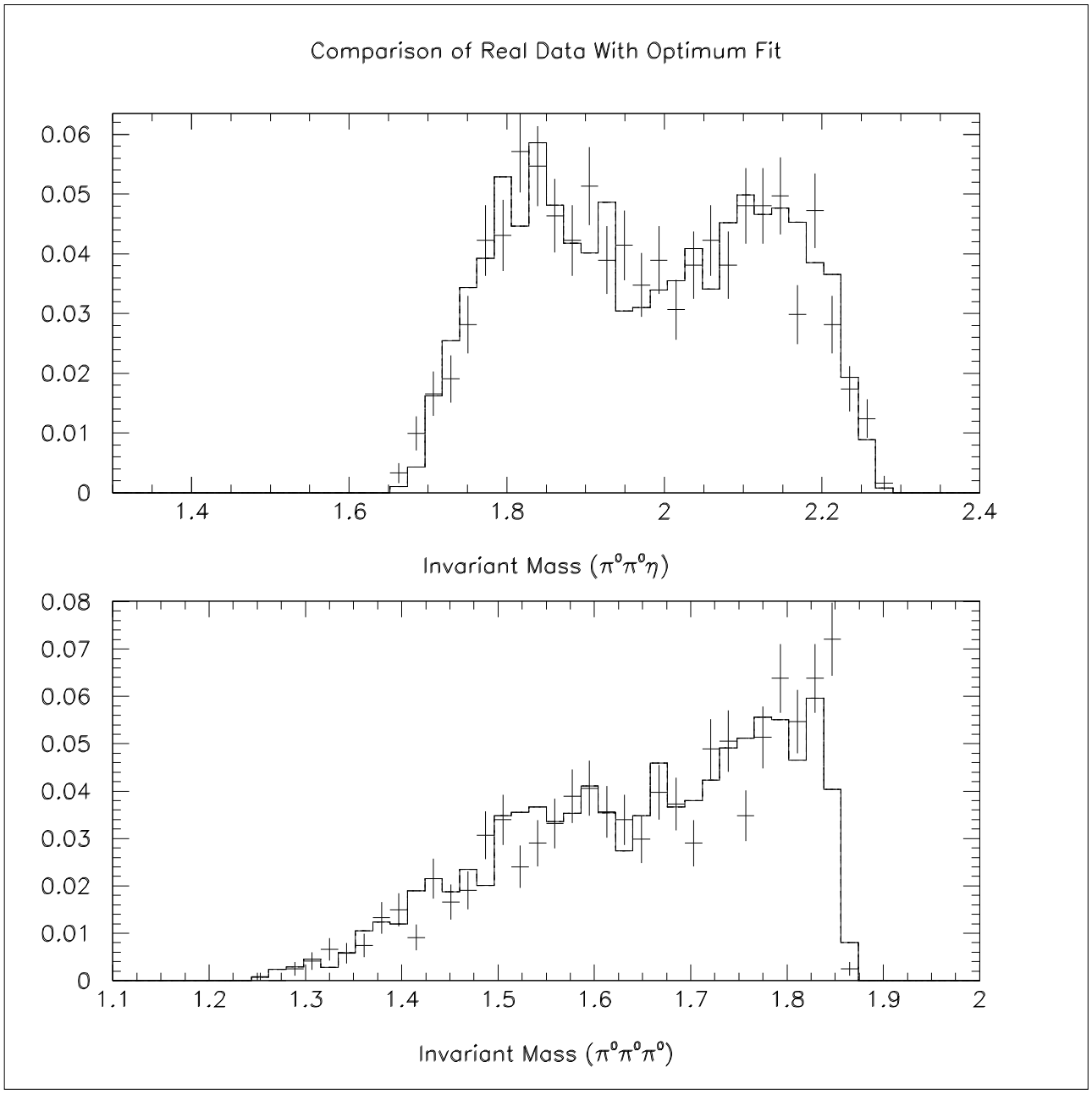

Figure 4.13: Comparison of real data with the optimum fit projections. These plots have the $(\pi^0\pi^0)$ combination in the $f_2(1270)$ mass region and the $(\pi^0\eta)$ masses are not in the $a_2(1320)$ mass region. Error bars represent the real data.

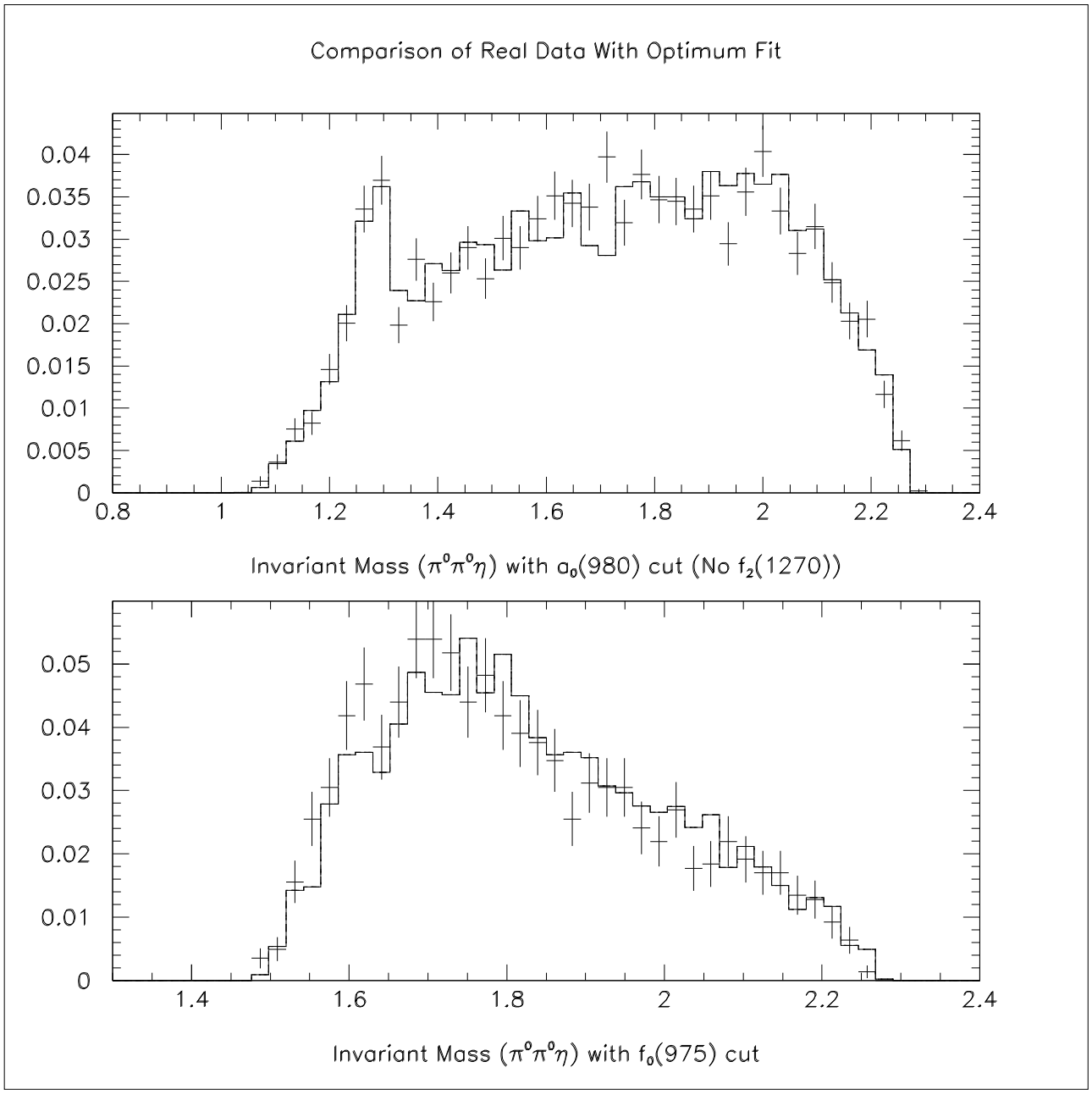

Figure 4.14: Top: Invariant mass $(\pi^0\pi^0\eta)$ for $(\pi^0\eta)$ combinations in the $a_0(980)$ mass region and the $(\pi^0\pi^0)$ not in the $f_2(1270)$ mass region. Bottom: Invariant mass $(\pi^0\pi^0\eta)$ for events with $(\pi^0\pi^0)$ in the $f_0(975)$ mass region.

Chapter 5

Concluding Comments

The aim of this analysis was to observe new $J^P=2^-$ states and therefore contribute to the search for the missing 2^- glueball candidate. This search for 2^- states uses $\bar{p}p \to \pi\pi\pi\eta$ Crystal Barrel data:

- $\bar{p}p \to \pi^+\pi^-\pi^0\eta$ at 1.20 GeV/c
- $\bar{p}p \to \pi^+\pi^-\pi^0\eta$ at 1.94 GeV/c
- $\bar{p}p \to \pi^0\pi^0\pi^0\eta$ at 1.20 GeV/c
- $\bar{p}p \to \pi^0\pi^0\pi^0\eta$ at 1.94 GeV/c.

The data have good mass resolution and are a rich source of resonances through a variety of decay channels. The use of invariant mass distributions and the comparison of real and Monte Carlo data provides a crude but effective method of searching for initial indications of new resonances. Discrepancies in the mass distributions have provoked a more thorough analysis to establish quantum numbers of the resonances. Both charged channel data sets contain a discrepancy in the comparison of the real and Monte Carlo data for the $\pi^+\pi^-\eta$ and $\pi^\pm\pi^0\eta$ invariant mass distributions. The discrepancy occurs for *all* distributions in the (1600-1800)MeV $\pi\pi\eta$ mass region. A second common feature of the charged channel data sets is the charged and neutral

ρ signal. Scatter plots of $(\pi\pi)$ versus $(\pi\eta)$ show enhancements due to $a_0(980)\rho$ and $a_2(1320)\rho$ signals above a large ρ band. A state decaying into $\eta\rho$ with zero orbital angular momentum between the η and ρ would have 2^{--} quantum numbers and produce a ρ band in a $(\pi\pi)$ versus $(\pi\eta)$ scatter plot. Therefore assuming that the enhancement in the (1600-1800)MeV $\pi\pi\eta$ mass region is due to $\eta\rho$, the $\pi^+\pi^-\pi^0\eta$ data shows great promise in the search for new 2^- states.

The $\pi^0\pi^0\pi^0\eta$ data also exhibits an interesting $\pi^0\pi^0\eta$ enhancement in the 1.94GeV/c data. This data set was chosen, in preference to the charged data, for spin analysis due to the limited number of isospin states. The maximum likelihood method was used to fit the $\pi^0\pi^0\pi^0\eta$ 1.94GeV/c data and the following channels were observed:

1. $\bar{p}p \rightarrow \mathrm{f}_2(1270).a_0(980) \rightarrow (\pi^0\pi^0)(\pi^0\eta)$
2. $\bar{p}p \rightarrow \sigma.a_2(1320) \rightarrow (\pi^0\pi^0)(\pi^0\eta)$
3. $\bar{p}p \rightarrow \pi^0 f_1(1285) \rightarrow \pi^0[\pi^0 a_0(980)] \rightarrow \pi^0\pi^0(\pi^0\eta)$
4. $\bar{p}p \rightarrow \sigma.a_0(980) \rightarrow (\pi^0\pi^0)(\pi^0\eta)$
5. $\bar{p}p \rightarrow \eta\pi_2(1670) \rightarrow \eta[\pi^0 f_2(1270)] \rightarrow \eta\pi^0(\pi^0\pi^0)$.

In addition to these channels it is necessary to include several more channels involving new or poorly established resonances. These resonances are discussed in the following sections.

5.1 $\eta_2(1650)$

The $\pi_2(1670)$ ($\mathrm{J}^{PC}=2^{-+}$) has a predicted isospin I=0 partner, the η_2. A natural candidate for this resonance has been observed with (1650$\pm$15) MeV mass and (180$\pm$75) MeV width. It is observed in the following decay channel:

- $\bar{p}p \rightarrow \pi^0\eta_2 \rightarrow \pi^0[\pi^0 a_2(1320)] \rightarrow \pi^0\pi^0(\pi^0\eta)$.

and contributes to the enhancement in the $\pi^0\pi^0\eta$ mass distribution. No additional decay modes have been observed and the quantum numbers are measured, without ambiguity, to be 2^{-+}. This channel interferes with channels 2, 5 and a second channel involving a new resonance with 1850 MeV mass and $J^{PC}=2^{-+}$.

5.2 $X(1850)$

The second new $J^{PC}=2^{-+}$ is observed to be produced at threshold in the channel:

- $\bar{p}p \to \pi^0 X(1850) \to \pi^0[\eta f_2(1270)] \to \pi^0\eta(\pi^0\pi^0)$.

The mass of the resonance is (1850±30) MeV and the width (225±75) MeV. Again, the $J^{PC}=2^{-+}$ quantum numbers are unambiguous and the $\pi^0[\eta f_2(1270)]$ decay is the only decay mode observed. The $\pi^0 X(1850)$ channel interferes with channels 1, 5 and $\pi^0\eta_2(1650)$.

The assignment of this state as the ninth member of the pseudotensor nonet is difficult. A possibility is that the $X(1850)$ is the same state as that observed in the MARK III data, Figure 4.8. The MARK III $J/\psi \to \gamma\pi^+\pi^-\eta$[45] data shows an enhancement in the $\pi^+\pi^-\eta$ mass distribution in the 1850MeV mass region. If these two states were the same then the $X(1850)$ must be a strong candidate for a 2^{-+} glueball.

5.3 $X(2135)$

A third channel required by the fit is:

- $\bar{p}p \to \pi^0 X(2135) \to \pi^0[\pi^0 a_2(1320)]$ and $\pi^0[\eta f_2(1270)]$.

The state, $X(2135)$, has a (2135±50) MeV mass and (250±50) MeV width with $J^{PC}=2^{++}$. Although many different spin states are predicted in this mass region,

2^{++} quantum numbers gave the only significant contribution. The most likely assignment of this state to a previously observed resonance is the $f_2(2175)$ observed by GAMS. By changing the optimum mass and width to those claimed by GAMS, the fit deteriorates by an insignificant amount.

5.4 Interference and the $\pi_2(1670)$

The effects of interference between channels has proven to enhance the sensitivity in measuring resonance masses. Although the prominent channels 1 and 2 appear to dominate the data and swamp the weaker channels, they are not a hindrance; they are important as interferometers. Phase variation due to interference helps to sharpen mass resolution and distinguish separate resonances with large widths and similar masses.

A complication in the fitting of the data is caused by the presence of the $\pi_2(1670)$. It's appearance in the data is not completely convincing. Evidence suggesting it's presence arises in the enhancement around 1670MeV of the $(\pi^0\pi^0\pi^0)$ mass distribution and large improvement to the fit when the $\eta\pi_2(1670)$ channel is included in the fit. Evidence suggesting a negligible contribution is seen in the $(\pi^0\pi^0)$ versus $(\pi^0\eta)$ scatter plot. The $\pi_2(1670)$ has a predominant decay mode into $f_2(1270)\pi^0$ and therefore the $f_2(1270)$ should appear as a band. Despite the $f_2(1270)a_0(980)$ region of enhancement, no clear $f_2(1270)$ band is seen. Having selected events with a $(\pi^0\pi^0)$ mass combination in the $f_2(1270)$ mass region, the corresponding $(\pi^0\pi^0\pi^0)$ mass distribution does not show any enhancement in the 1670MeV mass region.

Due to the evidence suggesting the presence of the $\pi_2(1670)$ and the fact that it is an established meson, the $\eta\pi_2(1670)$ channel is retained in the fit. The $\eta\pi_2(1670)$ channel has no effect on the observation of the $\eta_2(1650)$, $X(1850)$ and $X(2135)$ signal observations. The $\eta\pi_2(1670)$, $\pi^0X(1850)$ and $\pi^0X(2135)$ channels are able to mimic each other to some extent. This effect is seen when individual components are removed from the fit. Without the presence of the $\pi_2(1670)$, the significance of

the $X(1850)$ and $X(2135)$ signals is increased dramatically. However, even with the $\pi_2(1670)$, both the $X(1850)$ and $X(2135)$ provide highly significant contributions to the fit.

5.5 $TS(1635)$

A tentative signal, $TS(1635)$ is observed in the channel:

- $\bar{p}p \to \pi^0 TS(1635) \to \pi^0[\eta f_0(975)] \to \pi^0\eta(\pi^0\pi^0)$.

The mass is measured to be in the range (1625-1650) MeV. The quantum numbers giving the best fit are 0^{-+}, however, 1^{++} provides an improvement to the log likelihood which is almost as good. More statistics are necessary to resolve this ambiguity. A 0^{-+} with a mass in the region of 1635 MeV is most likely to be a radial excitation.

5.6 Future Work

The restriction in time only allowed a spin analysis of the $\bar{p}p \to \pi^0\pi^0\pi^0\eta$ at 1.94GeV/c data set. However, the results of this analysis prompts an analysis of the $\bar{p}p \to \pi^0\pi^0\pi^0\eta$ at 1.20GeV/c data in order to consolidate the observations of the $\eta_2(1650)$ and $X(1850)$ signals. It is expected that the spin analysis of the $\bar{p}p \to \pi^0\pi^0\pi^0\eta$ at 1.20GeV/c data should be relatively simple since the $\pi_2(1670)$ and high mass states decaying into $\pi^0\pi^0\eta$ are excluded due to the limits of phase space. Having completed a spin analysis of the $\pi^0\pi^0\pi^0\eta$ data, a search for 2^- states with isospin I=1 in the corresponding $\pi^+\pi^-\pi^0\eta$ data is made easier. The nature of the $X(1850)$ state must be verified by a spin analysis of the similar resonance observed in the MARK III data.

Appendix A

Scaling Factors, Confidence Levels and Pulls

This appendix presents the scaling factors, confidence level distributions and pulls from the kinematic fits.

A.1 Scaling Factors.

Tables ?? and A.1 show the scaling factors used in the analysis of the 0-prong data. The scaling factors for the Monte Carlo (MC) data were obtained using the $\pi^0\pi^0\pi^0\eta$ events. Scaling factors were applied to error magnitudes for parameters used in kinematic fits. The scaled photon errors used in kinematic fits were $\Delta\phi$, $\Delta\theta$ and $\Delta\text{Energy}_\gamma$. Also, despite the crystal calibration, it was necessary to scale the photon energies.

A.2 Confidence Level Distributions and Pulls.

In this section the confidence level (CL) distributions and the corresponding pull information are presented. For the 2-prong data sets, the CL distribution and hadronic split-off multiplicity provided by CBDROP are also shown.

Scaling Factor	July 0-Prong	Monte Carlo at 1.94GeV/c
γ SF($\Delta\phi$)	0.7900	1.050
γ SF($\Delta\theta$)	0.3500	0.450
γ SF(ΔE)	1.4000	1.450
γ SF(E)	1.0124	1.000

Table A.1: Scaling Factors for 0-Prong Data.

A.2.1 July 1992 0-Prong Data

Figure A.1 shows the CL distribution from the fits to energy-momentum, $\pi^0\pi^0\pi^0\gamma\gamma$ and $\pi^0\pi^0\pi^0\eta$. The flat distribution implies that overall, the errors were of the correct size.

Kinematic Fit to Z-Vertex at 1.94GeV/c					
Fit Parameter		Real Data		MC Data	
		Mean	Sigma	Mean	Sigma
γ	$\sqrt{E}$	0.204 ± 0.002	1.363 ± 0.002	0.359 ± 0.003	1.285 ± 0.003

Table A.2: Pulls for July 0-Prong Data.

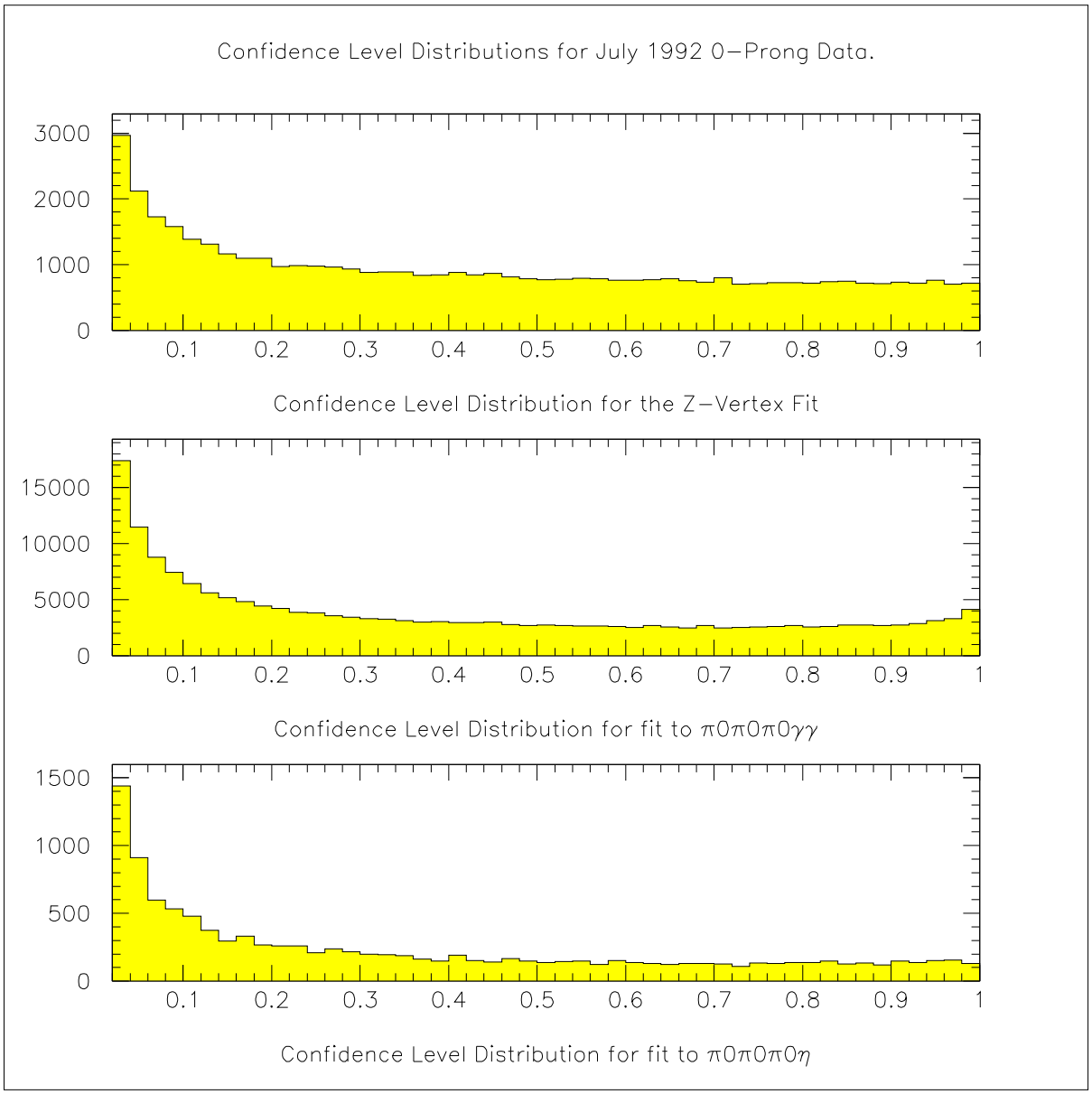

Figure A.1: CBKFIT: Confidence Level Distributions from the kinematic fitting of the July 1992 0-Prong Data.

Kinematic Fit to $\bar{p}p \to \pi^0\pi^0\pi^0\gamma\gamma$ at 1.94GeV/c					
Fit Parameter		Real Data		MC Data	
		Mean	Sigma	Mean	Sigma
γ	ϕ	0.000 ± 0.002	0.965 ± 0.001	-0.001 ± 0.003	1.049 ± 0.002
	θ	-0.001 ± 0.001	0.868 ± 0.001	-0.016 ± 0.003	0.955 ± 0.003
	$\sqrt{E}$	0.062 ± 0.002	0.995 ± 0.001	0.211 ± 0.003	0.986 ± 0.002

Table A.3: Pulls for July 0-Prong Data.

Kinematic Fit to $\bar{p}p \to \pi^0\pi^0\pi^0\eta$ at 1.94GeV/c					
Fit Parameter		Real Data		MC Data	
		Mean	Sigma	Mean	Sigma
γ	ϕ	0.004 ± 0.004	1.217 ± 0.003	0.000 ± 0.003	1.111 ± 0.003
	θ	0.014 ± 0.004	1.179 ± 0.003	-0.001 ± 0.003	1.073 ± 0.003
	$\sqrt{E}$	0.011 ± 0.004	1.146 ± 0.003	0.168 ± 0.003	1.004 ± 0.003

Table A.4: Pulls for July 0-Prong Data.

Bibliography

[1] F Abe *et al.*, FERMILAB-PUB-94/116-E May (1994)

[2] IJR Aitchison & AJG Hey, "Gauge Theories in Particle Physics" ed. DF Brewer (Adam Hilger)

[3] SL Glashow, Nucl. Phys. **22** 1961 (579)

[4] A Salam, "Elementary Particle Theory" ed. N Svartholm (Stockholm: Almqvist)

[5] S Weinberg, Phys. Rev. Lett. **19** 1967 (1264)

[6] M Gell-Mann & Y Ne'eman, Phys. Lett. **8** 1964 (214)

[7] M Aguilar-Benitez *et al.*, Rev. of Particle Properties, Phys. Rev. **D 45** (1992)

[8] T de Grand, RL Jaffe, K Johnson and J Kiskis, Phys. Rev. **D12**, 2060, (1975)

[9] NN Achasov, SA Devyanin and GN Shestakov, Sov. Phys. Usp., **27**, 161, (1984)

[10] R Kokoski and N Isgur, Phys. Rev., **D35**, 907, (1987)

[11] J Gasser and H Leutwyler, Nucl. Phys., **B250** 465,517 and 539 (1985)

[12] AJG Hey, Surv. High Energy Physics, **5**, 287, (1987)

[13] F Close, "Spectroscopy of Light and Heavy Quarks" Ed. U Gastaldi, R Klapisch & F Close

[14] M Poulet, "Exotic Mesons" First Biennial Conf. on Low Energy Antiproton Physics., World Scientific Publishing Co. (1991)

[15] F Close, AIP Conf. Proc. **185** ed. SU Chung, Brookhaven (1988)

[16] FG Binon, Nuclear Physics B (Proc. Suppl.) **8** 24 (1989)

[17] RL Jaffe & K Johnson, Phys. Lett. **60B**, 201, (1976)

[18] VV Anisovich *et al.*, Phys. Lett. **322**, 431, (1994)

[19] M Burchell, CERN-PPE/92-158 September (1992)

[20] C Amsler *et al.*, Nuclear Instruments and Methods in Physics Research, **A321**, 69-108, (1992)

[21] LeCroy, Multi Wire Proportional Chamber System.

[22] H. Drumm *et al.*, Nucl. Instr. and Meth. **176**, 333, (1980)

[23] LeCroy, Fast Encoding and Readout System.

[24] LeCroy, 2282 High Density ADC Data Acquisition System.

[25] R. Brun and J. Zoll, ZEBRA user guide, CERN Program Library Q100, (1987)

[26] K. Braune, The Fast Cluster Encoder, CB-Note 41, (1986), Unpublished.

[27] G. Folger and M. Doser, Crystal Barrel Offline Reconstruction Software, CB-Note 121, (1993), Unpublished.

[28] C. Meyer, Crystal Barrel Chamber Reconstruction Software, CB-Note 93, (1991), Unpublished.

[29] C. Meyer, Crystal Barrel Chamber Reconstruction Software: User Guide., CB-Note 123, (1991), Unpublished.

[30] F.H. Heinsius and T. Kiel, Crystal Barrel Crystal Data Reconstruction Software, CB-Note 92, (1991), Unpublished.

[31] M. Burchell, Crystal Barrel Global Tracking Particle Bank Structure, CB-Note 118, (1991), Unpublished.

[32] R. Veenhof, CERN program library W5050 (1989)

[33] N. Hessey, Split-off recognition with Dolby-C, CB-Note 199, (1992), Unpublished.

[34] C. Meyer, User Guide for CBDROP - A Charged Split-Off Suppression Package, CB-Note 191, (1992), Unpublished.

[35] P. Hidas and G. Pinter, Kinematic Fitting Software, CB-Note 138, (1993), Unpublished.

[36] Program 353QH, CERN Program Library (1987)

[37] W Chinowsky, G Goldhaber *et al.*, Phys. Rev. Letters **9**, 330 (1962)

[38] G Goldhaber, W Chinowsky *et al.*, Phys. Letters **6**, 62 (1963)

[39] BS Zou and DV Bugg, Phys. Rev., **D48**, 3948, (1993)

[40] A subroutine for Fitting the χ^2 and Maximum Likelihood Function (FUMILI, LIKELM), CERN Program Library, **D510** 1971.

[41] C Bourrely, E Leader and J Soffer, Phys. Reports, **59**, Number 2, March 1980.

[42] YU D Prokoshkin, Hadron 89 Conference. p27

[43] K Karch *et al.*, Phys Lett. **B249** 353 (1990)

[44] SI Bityukov *et al.*, Protvino preprint IFVE-91-26

[45] W Stockhausen, SLAC preprint SLAC-PUB-4026 July (1986)